AD-A259 085

DNA-TR-92-37-V2

Chernobyl Doses
Volume 2—Conifer Stress Near Chernobyl Derived from Landsat Imagery

Gene E. McClellan
Terrence H. Hemmer
Ronald N. DeWitt
Pacific-Sierra Research Corporation
12340 Santa Monica Boulevard
Los Angeles, CA 90025-2587

December 1992

DTIC
ELECTE
DEC 22 1992
S E D

Technical Report

92-32436

92 19 22 018

DISCLAIMER NOTICE

THIS DOCUMENT IS BEST QUALITY AVAILABLE. THE COPY FURNISHED TO DTIC CONTAINED A SIGNIFICANT NUMBER OF COLOR PAGES WHICH DO NOT REPRODUCE LEGIBLY ON BLACK AND WHITE MICROFICHE.

DISTRIBUTION LIST UPDATE

This mailer is provided to enable DNA to maintain current distribution lists for reports. (We would appreciate your providing the requested information.)

☐ Add the individual listed to your distribution list.

☐ Delete the cited organization/individual.

☐ Change of address.

NAME: _____

ORGANIZATION: _____

OLD ADDRESS	CURRENT ADDRESS
_____	_____
_____	_____
_____	_____

TELEPHONE NUMBER: (____) _____

DNA PUBLICATION NUMBER/TITLE	CHANGES/DELETIONS/ADDITIONS, etc.) *(Attach Sheet if more Space is Required)*
_____	_____
_____	_____
_____	_____

DNA OR OTHER GOVERNMENT CONTRACT NUMBER: _____

CERTIFICATION OF NEED-TO-KNOW BY GOVERNMENT SPONSOR (if other than DNA):

SPONSORING ORGANIZATION: _____

CONTRACTING OFFICER OR REPRESENTATIVE: _____

SIGNATURE: _____

CUT HERE AND RETURN

DEFENSE NUCLEAR AGENCY
ATTN: TITL
6801 TELEGRAPH ROAD
ALEXANDRIA, VA 22310-3398

REPORT DOCUMENTATION PAGE

Form Approved
OMB No. 0704-0188

1. AGENCY USE ONLY (Leave blank)	2. REPORT DATE	3. REPORT TYPE AND DATES COVERED
	921201	Technical 870929 – 920228

4. TITLE AND SUBTITLE

Chernobyl Doses
Volume 2 — Conifer Stress Near Chernobyl Derived from Landsat Imagery

6. AUTHOR(S)

Gene E. McClellan, Terrence H. Hemmer, and Ronald N. DeWitt

5. FUNDING NUMBERS

C   - DNA 001-87-C-0104
PE - 62715H
PR - RM
TA - RH
WU - DH026130

7. PERFORMING ORGANIZATION NAME(S) AND ADDRESS(ES)

Pacific-Sierra Research Corporation
12340 Santa Monica Boulevard
Los Angeles, CA 90025-2587

8. PERFORMING ORGANIZATION REPORT NUMBER

PSR Report 2250

9. SPONSORING/MONITORING AGENCY NAME(S) AND ADDRESS(ES)

Defense Nuclear Agency
6801 Telegraph Road
Alexandria, VA 22310-3398
RARP/Young

10. SPONSORING/MONITORING AGENCY REPORT NUMBER

DNA-TR-92-37-V2

11. SUPPLEMENTARY NOTES

This work was sponsored by the Defense Nuclear Agency under RDT&E RMC Code B4662D RM RH 00038 STRP 3500A 25904D.

12a. DISTRIBUTION/AVAILABILITY STATEMENT

Approved for public release; distribution is unlimited.

12b. DISTRIBUTION CODE

13. ABSTRACT *(Maximum 200 words)*

This volume presents Landsat Thematic Mapper imagery of the area surrounding the Chernobyl Nuclear Reactor Station and derives quantitative estimates of the spatial extent and time progression of stress on coniferous forests resulting from the 26 April 1986 reactor explosion and release of radioactive material. Change detection between pre- and postaccident images demonstrates convincingly that remote sensing of the spectral reflectance of coniferous forests in visible and infrared wavelengths at moderate spatial resolution (30 meters) will detect the effects of large radiation doses to the forest canopy.

This work was initiated at a time when the expectation for direct data from the Soviet Union on local, accident-induced radiation levels was limited and the satellite data provided an alternative source. Although information exchange with the former Soviet Union has improved dramatically, the results of this report are important, since they prove the feasibility of large-scale, spectral response measurements on radiation-exposed pine trees in a natural environment. Volume 1 presents the derivation of radiation doses from the imagery reviewed in this volume, describes changes in spectral reflectivity of the affected trees as a function of dose and time, and discusses the military operational implications of these results.

14. SUBJECT TERMS

Chernobyl	Forest Damage	Landsat
Change Detection	Conifer Stress	Fallout
Ionizing Radiation	Multispectral Imagery	

15. NUMBER OF PAGES

80

16. PRICE CODE

17. SECURITY CLASSIFICATION OF REPORT	18. SECURITY CLASSIFICATION OF THIS PAGE	19. SECURITY CLASSIFICATION OF ABSTRACT	20. LIMITATION OF ABSTRACT
UNCLASSIFIED	UNCLASSIFIED	UNCLASSIFIED	SAR

CLASSIFIED BY:

N/A since Unclassified.

DECLASSIFY ON:

N/A since Unclassified.

PREFACE

This volume is the second in a series of three volumes composing the final report to the Defense Nuclear Agency (DNA) for contract DNA001-87-C-0104, Chernobyl Doses. This document was prepared by investigators at Pacific-Sierra Research Corporation (PSR) as a topical report for that contract but is being published as a volume of the final report. It describes the acquisition and processing of Landsat imagery of the area containing the Chernobyl Nuclear Reactor Station and presents the exploratory analysis of the imagery using PSR's proprietary Hyperscout™ change detection algorithm. Volume 1, *Analysis of Forest Canopy Radiation Response from Multispectral Imagery and the Relationship to Doses*, presents the analytical work that connects these multispectral observations of pine forests in the images to the nuclear radiation dose received by the trees as a consequence of the reactor accident of 26 April 1986. Volume 3, *Habitat and Vegetation Near the Chernobyl Nuclear Reactor Station*, presents a detailed exposition on the soil, climate, and vegetation of the Poles'ye region of the Ukraine and Belorussia with emphasis on the area around Chernobyl.

The authors wish to acknowledge Frank Thomas and George Anno of PSR, who recognized the potential for remote sensing of radiation-damaged foliage around Chernobyl; Wayne Hallada and the late Quentin Wilkes of PSR, who arranged the necessary equipment and image acquisitions; and finally, the skillful manuscript preparation by Kathy Howell and Sunny Wiard.

The authors wish to acknowledge the technical monitor of this project, Robert W. Young of DNA's Radiation Policy Division, for his support and encouragement during this work. Dr. Young was assisted first by MAJ Bruce West and then by MAJ Robert Kehlet. The authors also wish to acknowledge Dr. Marvin Atkins and Dr. David Auton of DNA whose interest made this work possible.

DTIC QUALITY INSPECTED 2

Accesion For		
NTIS CRA&I	☑	
DTIC TAB	☐	
Unannounced	☐	
Justification		
By		
Distribution /		
Availability Codes		
Dist	Avail and / or Special	
A-1		

™Hyperscout is a registered trademark of Pacific-Sierra Research Corporation.

CONVERSION TABLE

Conversion factors for U.S. customary to metric (SI) units of measurement

To Convert From	To	Multiply
angstrom	meters (m)	1.000 000 X E-10
atmosphere (normal)	kilo pascal (kPa)	1.013 25 X E+2
bar	kilo pascal (kPa)	1.000 000 X E+2
barn	meter^2 (m^2)	1.000 000 X E-28
British Thermal unit (thermochemical)	joule (J)	1.054 350 X E+3
calorie (thermochemical)	joule (J)	4.184 000
cal (thermochemical)/cm^2	mega joule/m^2(MJ/m^2)	4.184 000 X E-2
curie	giga becquerel (GBq)*	3.700 000 X E+1
degree (angle)	radian (rad)	1.745 329 X E-2
degree Fahrenheit	degree kelvin (K)	$t_K=(t°f + 459.67)/1.8$
electron volt	joule (J)	1.602 19 X E-19
erg	joule (J)	1.000 000 X E-7
erg/second	watt (W)	1.000 000 X E-7
foot	meter (m)	3.048 000 X E-1
foot-pound-force	joule (J)	1.355 818
gallon (U.S. liquid)	meter^3 (m^3)	3.785 412 X E-3
inch	meter (m)	2.540 000 X E-2
jerk	joule (J)	1.000 000 X E+9
joule/kilogram (J/Kg) (radiation dose absorbed)	Gray (Gy)	1.000 000
kilotons	terajoules	4.183
kip (1000 lbf)	newton (N)	4.448 222 X E+3
kip/inch^2 (ksi)	kilo pascal (kPa)	6.894 757 X E+3
ktap	newton-second/m^2 (N-s/m^2)	1.000 000 X E+2
micron	meter (m)	1.000 000 X E-6
mil	meter (m)	2.540 000 X E-5
mile (international)	meter (m)	1.609 344 X E+3
ounce	kilogram (kg)	2.834 952 X E-2
pound-force (lbf avoirdupois)	newton (N)	4.448 222
pound-force inch	newton-meter (N·m)	1.129 848 X E-1
pound-force/inch	newton/meter (N/m)	1.751 268 X E+2
pound-force/foot^2	kilo pascal (kPa)	4.788 026 X E-2
pound-force/inch^2 (psi)	kilo pascal (kPa)	6.894 757
pound-mass (lbm avoirdupois)	kilogram (kg)	4.535 924 X E-1
pound-mass-foot^2 (moment of inertia)	kilogram-meter^2 (kg·m^2)	4.214 011 X E-2
pound-mass/foot^3	kilogram/meter^3 (kg/m^3)	1.601 846 X E+1
rad (radiation dose absorbed)	Gray (Gy)**	1.000 000 X E-2
roentgen	coulomb/kilogram (C/kg)	2.579 760 X E-4
shake	second (s)	1.000 000 X E-8
slug	kilogram (kg)	1.459 390 X E+1
torr (mm Hg. 0°C)	kilo pascal (kPa)	1.333 22 X E-1

*The becquerel (Bq) is the SI unit of radioactivity: Bp = 1 event/s.

**The Gray (Gy) is the SI unit of absorbed radiation.

TABLE OF CONTENTS

FIGURES

TABLES

SECTION 1

INTRODUCTION

On 26 April 1986, at 1:24 a.m. local time, the Chernobyl nuclear reactor number four blew up. This report describes the research of investigators at Pacific-Sierra Research Corporation (PSR) in studying the effects of radioactivity deposited in the immediate area by the accident. Specifically, it describes the quantitative analysis of the multispectral (MS) imagery of the area surrounding the Chernobyl nuclear reactor.

1.1 BACKGROUND.

Before the explosion only theoretical models suggested our ability to monitor remotely the effects caused by widely distributed large doses of radiation. The sensitivity of vegetation to large doses of radiation had been measured only in the lab and in small-scale field experiments. The Chernobyl accident provides an opportunity to observe both short- and long-term effects of high radiation dose on plants. The large spatial scale of the affected area allows us to evaluate the utility of remotely sensed multispectral imagery in quantifying the extent of damage to foliage and in estimating the radiation dose that was deposited by the accident.

The accident occurred before the changes of Glasnost could be taken for granted. Indeed, because the initial tendency of Soviet authorities was to deny the accident, there was little basis for anticipating sufficient and accurate information from Soviet sources. Therefore, any independent source of information that could augment or verify the information released by Soviet authorities seemed desirable. In particular, some method for obtaining an independent assessment of dose was regarded to be of primary interest.

The most obvious method was to use remote sensors. Because overflights of Soviet territory were deemed impossible, the remote sensor would have to be in a low-altitude orbit. The remote measurement of radiation at this distance is prevented by atmospheric attenuation. On the other hand, the remote measurement of the *effects* of the radiation on vegetation was possible with the existing satellite sensor mix. Two of these sensors were the Landsat Thematic Mapper (TM) and SPOT maintained by the United States and France, respectively. Because both of these are commercial systems, data is readily available. In effect, vegetation provides an on-site biological dosimeter that can be read remotely with multispectral imagery.

Such remote sensing of vegetation stress is an important scientific endeavor contributing to early detection of the effects of major disasters such as Chernobyl as well as the chronic effects of major pollution sources. Analysis of imagery of the Chernobyl accident provides a benchmark for this capability.

1

1.2 ORGANIZATION OF REPORT.

Following this introduction, Section 2 presents the physical basis for the spectral detection of vegetation stress. Section 3 describes the usual approaches to the detection of stress. Section 4 follows with a description of the sensor, imagery selection criteria, and preprocessing requirements. Section 5 presents the imagery, including detected indications of vegetation stress. Since limited ground truth (radiation measurements) was published by the Soviets, this ground truth can be compared to the detected stress. Section 6 presents this comparison. Section 7 reiterates salient features and compares this work with other similar work. Section 8 contains concluding remarks and makes recommendations for continuation and improvements.

SECTION 2

THE PHYSICAL BASIS FOR THE SPECTRAL DETECTION OF VEGETATION STRESS

We have asserted that dose estimates for the Chernobyl area can be obtained by monitoring the effects of the radiation on indigenous vegetation. In making this assertion, we assume that the accident sufficiently dosed the vegetation to invoke a response detectable in the spectral regions monitored by satellite sensors. This section provides the justification for these assumptions.

We simplify the analysis by concentrating on only one type of plant community. Three criteria governed the selection of the type of plant community to be monitored. First, our desire to determine the radiation dose dictated a plant type relatively sensitive to radiation. Second, the selection of a plant species pervading the area of interest allows estimates of the areal extent of the radiation effects. Third, because the time scale of the manifestation of stress could not be anticipated, we desired a plant type subject to little seasonal variation .

Coniferous forests meet all three requirements. Table 2-1 shows that coniferous forests are very sensitive to radiation. The extensive forests located throughout the area around the Chernobyl reactor complex comprise predominantly conifers, with common pine, *Pinus sylvestris* (see Volume III of this report1) the primary species. Finally, conifers show relatively little seasonal spectral variation compared to deciduous trees. However, seasonal changes in illumination and variations in the canopy closure of intermixed deciduous species, as well as changes caused by the maturing of the predominant foliage, vary the observed reflectance spectrum somewhat from season to season.

Table 2-1. Estimated short-term radiation exposures required to damage various plant communities (Whicker and Fraley, 1974).

Community type	Exposures to produce (kR)		
	Minor effects	*Intermediate effects*	*Severe effects*
Coniferous forest	0.1-1	1-2	>2
Deciduous forest	1-5	5-10	>10
Shrub	1-5	5-10	>10
Tropical rain forest	4-10	10-40	>40
Grassland	8-10	10-100	>100
Moss-lichen	10-50	50-500	>500

3

Before presenting the spectral manifestations of stress, we discuss the spectral characteristics of healthy vegetation, with emphasis on those areas of the spectrum that can be monitored by either Landsat or SPOT. In the visible region of the electromagnetic spectrum extending from wavelengths of 0.4 to 0.7 micrometers (μm), chlorophyll absorption (Hoffer, 1978) dominates the reflectance spectra of healthy vegetation. Chlorophyll absorbs throughout this region, but it absorbs less in the green than in the blue or red. This preferential absorption causes the green color of healthy vegetation.

The infrared (IR) region of the spectrum comprises several subregions: the near infrared (NIR); short-wave infrared (SWIR); mid-wave IR (MWIR); and thermal or long-wave IR (LWIR). The wavelength interval defining each of these spectral regions varies from author to author. This report defines the NIR region to extend from about 0.7 μm to 1.3 μm. In this subregion, the spongy mesophyll tissue in the interior of the leaves causes the foliage to reflect strongly, typically as much as 45 to 50 percent of incident illumination. The SWIR spectral region, from approximately 1.5 μm through 2.5 μm, includes two absorption features of the leaf water content, reducing the foliage spectral reflectance. Neither Landsat nor SPOT are sensitive in the MWIR, which extends from about 3 to 5 μm. The LWIR includes electromagnetic radiation from 8 μm to 12 μm and beyond. Because at terrestrial temperatures most materials have spectral characteristics in the LWIR that tend to be emissive rather than reflective, this band is referred to as the thermal IR. Thus, in this region the temperature and the emissivity of the vegetation determines its spectral response. Under normal conditions, transpiration and efficient heat exchange keep the temperature of foliage close to air temperature (Estes, 1983; Weibelt and Henderson, 1976).

The spectral manifestations of stress depend strongly on the cause of the stress (Estes, 1983). For example, moisture stress initially results in increased reflectance in the SWIR, because there is less water to absorb the infrared radiation (Hoffer, 1978). Desiccation of pine needles to approximately 48 percent of fresh weight reduces NIR reflectance dramatically, while SWIR reflectance continues to rise (Westman and Price, 1988). An expected lack of cooling by transpiration would allow stressed foliage to be warmed by sunlight to temperatures higher than those of healthy vegetation and would result in relatively higher emissions in the thermal IR. If the moisture stress impedes chlorophyll production, the reflectivity in the visible can also be expected to increase. The spectral properties of other pigments in the leaf may now become dominant, resulting in a yellowish or reddish color.

Cellular damage results in a marked decrease in the reflectance in the NIR. Little or no change in the visible is expected unless the damage reduces chlorophyll content or causes the production or destruction of other pigments.

Unfortunately, the specific spectral manifestations of ionizing radiation damage to foliage are not well known. However, one form of radiation-induced stress may be at least partially

4

predictable. The spectral reflectance of new pine needle growth is significantly higher than that of old pine needle growth at all wavelengths (Wolfe and Zissis, 1978). If the radiation stress results in either reduced or accelerated growth of new needles (an effect expected to be highly dependent on dose), then this deviation may be detectable.

SECTION 3

QUANTITATIVE ANALYSIS OF MULTIDATE IMAGERY

The problem of identifying stress in imagery can be approached in two ways. The first approach assumes that stressed vegetation has unique spectral signatures, and that these spectral signatures are sufficiently different from the spectral signatures of healthy vegetation that a suitable spectral transformation can be applied to the image to render stressed vegetation readily apparent to the image analyst. For example, Johnson (Johnson, 1989) developed a phenomenologically based image-enhancement transformation designed to detect a specific spectral manifestation of stress. Section 7 discusses this transformation in more detail.

The other approach to identifying stress in imagery attempts to exploit the additional information content of multidate imagery. Multidate algorithms generally fall into two major categories: change detection algorithms and dynamic-system algorithms. Change detection algorithms tend to ignore explicit spectral properties and concentrate only on differences from date to date, except insofar as the spectral properties are associated with particular kinds of ground covers that manifest the change. Spectral properties are occasionally used, but only at a later stage to characterize the detected change. Dynamic-system algorithms tend to retain most of the spectral information.

3.1 FACTORS AFFECTING THE UTILITY OF MULTIDATE IMAGERY.

An accurate assessment of the fallout from the Chernobyl nuclear reactor accident through its effect on coniferous forests can be made only if a number of rather stringent requirements are met. First, there must be a sensor capable of detecting and tracking the changes in the spectral properties of the vegetation. Second, all unrelated factors that affect the spectral properties of vegetation on an image-to-image basis must be normalized out so that direct multidate comparisons can be made. Third, the data must be very accurately registered. Fourth, data must be available at frequent enough intervals.

Numerous extraneous factors can affect the comparison of two or more images. Some of these factors are environmental (e.g., haze, humidity, sun angle, and cloud cover). Others are instrumental (e.g., view angle, pointing accuracy, spectral sensitivities, and resolution). Even if the same sensor at the same relative position at the same time of day is used, the differences between images can be quite large. Either the images must be corrected for these differences, or an algorithm that is insensitive to these extraneous differences must be used.

Because multidate algorithms use the spectral information for the same ground point on two or more dates, the images must be registered (geocoded). Geocoding processes the images from all

dates so that the picture element (pixel) at the same position in each date's image corresponds to a common area on the ground. Registration accuracy is of fundamental importance in the analysis of multidate imagery. Variations in the satellite orbit, pointing accuracy, jitter, and numerous other reasons make exact registration impossible, but registration to within a fraction of a pixel width is often possible.

Finally, multidate image analysis requires that images be collected at time intervals that are small compared to the time scale of the process being monitored. In the case of radiation stress, the local radiation dose determines that time scale and causes it to vary from one place to another according to the distribution of the radiation fallout. This variation imposes a requirement for frequent images to monitor the development of stress in highly contaminated areas, but less frequent imaging will suffice in the regions of lesser contamination. Because cloud cover often renders satellite data useless, data collections at time intervals smaller than the time scale of the stress development process must be attempted.

3.2 SELECTION OF AN ALGORITHM.

The approach first envisioned for this project involved tracking the spectral properties of large areas of forest as a function of time. This approach falls in the dynamic-system category. Large areas of the forest would be delineated by polygons for the analysis. We can fit multivariate normal distributions to the measurements taken on each date within each polygon in the following manner. For a given ground pixel, there is an intensity value measured in each band, and these intensities can be formed into an ordered set called the *pixel vector*. A polygon's mean intensity vector can be computed by averaging the pixel vectors over all pixels within the polygon. Once the polygon's mean intensity vector has been determined, there can be computed for each pixel a deviation vector (representing a pixel intensity vector's departure from the mean vector) by simply subtracting the polygon's mean intensity vector from the pixel vector. The polygon's covariance matrix can then be computed by forming a matrix comprising all pairings of the intensities for each pixel deviation vector and then averaging these matrices over all pixels in the polygon (Swain, 1978). The resulting mean intensity vector and intensity covariance matrix suffice to characterize a multivariate normal distribution for that particular polygon for that particular day. This process would be performed for all polygons for all images.

Next, a reference image (date) would be chosen, and quantitative methods would be used to identify the spectral deviations of each forested area from the spectral properties of the same forested area on the reference image. This approach requires the removal from the multidate images of any variations that are not directly related to stress. Many of these variations can be removed by rescaling the date-of-interest image (the image for which the stress is to be calculated) to the reference image. This rescaling can significantly reduce the effects of seasonal variations in

7

the incidence angle of solar illumination. If this rescaling is done on a band-by-band basis, rescaling can also reduce the effects of those variations in the atmospheric condition that are uniform over the entire area of interest. Rescaling cannot reduce the effects of variation in cirrus cloud density or other local atmospheric conditions.

To perform the rescaling, we selected several forest "training sites." A forest "training site" is a forested area that is assumed to be spectrally identical, before solar and atmospheric variations, on the two dates. Statistics were computed for each of the training sites. Unfortunately, the scale factors that were computed from the mean vectors were different for different training sites. This suggests that there were significant spectral variations across the image that were not related to stress and could not be normalized out. Further, rescaling by a multiplicative constant concomitantly requires the rescaling of the covariance matrix elements by the square of the corresponding multiplicative constant for diagonal elements and by the products of multiplicative constants for the off-diagonal elements. The resulting rescaled covariance matrices did not match the reference date covariance matrices. Because these difficulties would adversely affect the sensitivity, and hence the usefulness of the ensuing analysis, this approach was abandoned.

Fortunately, in the interim PSR developed in an independent research and development (IR&D) project, an extremely sensitive method of stress detection, the Hyperscout™ algorithim. Because of its sensitivity, this algorithm was used in the quantitative portion of the study. In addition, several procedures for identifying the spectral signatures that correspond to stressed vegetation were developed.

™Hyperscout is a registered trademark of Pacific-Sierra Research Corporation.

SECTION 4

THEMATIC MAPPER IMAGERY

4.1. INTRODUCTION TO THE THEMATIC MAPPER.

The Landsat Thematic Mapper (TM) sensor collects data in seven bands in 4 regions of the electromagnetic spectrum (see Table 4-1): three visible; one near infrared (NIR); two short-wave infrared (SWIR); and one thermal infrared (Engel, 1984). That is, seven images were obtained: one through each of the seven spectral band filters. Each region of the spectrum supplies information on different manifestations and levels of stress as discussed in Section 2.

A comment on the numbering of the TM bands may help prevent confusion. As discussed above and displayed in Table 4-1, the numbering of the bands is not strictly in order of increasing wavelength.[1] Specifically, *band 6 is out of sequence.* In order of increasing wavelength, the bands are: 1 through 5, 7, and then 6.

Table 4-1. Landsat TM spectral bands.

Band number	Spectral region	Wavelength band (microns)	IFOV* (meters)	Stress sensitivities
1	Visible	0.45-0.52	30	Pigmentation changes (Especially chlorophyll)
2	Visible	0.52-0.60	30	" "
3	Visible	0.63-0.69	30	" "
4	NIR	0.76-0.90	30	Plant structure damage
5	SWIR	1.55-1.75	30	Moisture stress
7	SWIR	2.08-2.35	30	" "
6	Thermal	10.40-12.50	120	Plant heat stress

*Instantaneous field of view

---

[1]Thematic Mapper Simulator (TMS) data, on the other hand, is sequential (i.e., TMS bands 6 and 7 are reversed from TM bands 6 and 7). No further reference to TMS data is made in this study. Band numbers will always refer to TM band numbers and, therefore, will be out of wavelength sequence.

A TM image is built up by scanning a sensor that has an instantaneous field of view (IFOV) that when projected on the ground measures 30 meters (m) in bands 1 through 5 and 7, and 120 m in band 6. During processing, all bands are usually resampled to 28.5 m. Geocoded products, such as those used in this study, are resampled to 25 m.

A frequently encountered misconception is that because the smallest resolvable object can be no smaller than a pixel, no information on a scale smaller than a pixel can be extracted. In fact, information from objects much smaller than the pixel dimensions can sometimes be extracted. One dramatic example of this was the identification of natural gas flarings in the NOAA-6 Advanced Very High Resolution Radiometer (AVHRR) data (Matson and Dozier, 1981). The pixel size of the NOAA-6 AVHRR sensor was 1.1 kilometer (km) on a side at nadir, while the dimensions of natural gas flarings are clearly only a very small fraction of that size. Further, for AVHRR pixels only partially contaminated by cloud, it was possible to determine both the fraction of pixel occupied by the cloud and the brightness temperature of the cloud. How is this possible? In the case of the natural gas flarings, the flaring was many orders of magnitude brighter than the background. Thus, the overall brightness of a pixel was affected although the pixel was orders of magnitude larger than the flarings. In the case of cloud contamination, the key is that the data are multispectral. Because there were two "thermal" bands (one MWIR and one thermal) on the AVHRR instrument, two intensity levels were recorded for each pixel. In some cases these intensity levels may be used to extract information on a subpixel scale. The more bands collected, the more subpixel information that can be extracted.

The Landsat 4 and 5 satellites are in 705-km sun-synchronous orbits (Irons, 1985). The descending node equatorial crossing time (local time) is 9:45 a.m. Thus, all Landsat images are acquired in the morning at about the same local time. This minimizes the scene-to-scene image variations caused by the solar illumination angle.

The TM sensor collects a 185-km wide swath centered at nadir. To completely cover the Earth's surface, 233 orbits are required. Because the orbit period is 98.9 minutes, 16 days are required to complete the 233 orbits. Thus, neglecting overlap, each area on the ground can be imaged no more frequently than once every 16 days. This 16-day repeat cycle of the TM is not frequent enough to monitor the areas receiving the highest dose, especially when allowance was made for cloud cover. Fortunately, because the image swaths overlap, a TM image of the Chernobyl area could be acquired every 7 or 9 days. The very high probability of cloud cover is still a problem for which there is no solution. For areas receiving lower doses, the 7- or 9-day repeat cycle is probably frequent enough to monitor radiation stress.

4.2 MOTIVATION FOR USE OF THEMATIC MAPPER IMAGERY.

Early detection and continuous monitoring of the coniferous tree stress was critical to the accuracy of the exposure estimates. Thus, the sensor needs to be sensitive to those regions of the spectrum that most clearly exhibit the effects of radiation stress. Unfortunately, the spectral manifestations of radiation stress were uncertain. This uncertainty was the primary motivation for the use of TM data; TM collects data in four regions of the spectrum, while SPOT collects data in only two regions of the spectrum. Thus, even though SPOT has a much higher spatial resolution (10-m panchromatic, 20-m multispectral), it does not have the spectral range of TM.

PSR's Hyperscout change detection algorithm is theoretically independent of the sensor, provided that any sensor that is used collects data in the appropriate spectral regions.

4.3 IMAGE SELECTION AND PROCUREMENT.

To select images for analysis, we first obtained a list of all TM acquisitions from EOSAT Corporation. Second, to avoid purchasing a large number of images that were not usable because of cloud cover, we identified those images collected in the area around Chernobyl that were cloud free. The simplest approach to identifying cloud free images would have been to use the automatic cloud cover assessment on the Landsat acquisition listing. Unfortunately, this number represents the cloud cover percentage over the entire scene (an area which is 100 nautical miles (nmi) on a side) and not the cloud cover over the immediate area of interest. Even if the cloud cover rating for the scene is 80 percent or more, it is still possible that the area of interest is cloud free. Conversely, a cloud cover rating of 10 percent did not guarantee that the area of Chernobyl was cloud free. Thus, a more localized analysis was desirable. For this study, cloud contamination was assessed in two ways. First, Multispectral Scanner data, which are recorded simultaneously with TM data, were reviewed at the (MSS) microfilm library located at EOSAT Corporation's headquarters in Lanham, Maryland, and observations on image quality and cloud cover contamination were recorded (see Table 4-2). Next, black and while (B&W) prints were obtained as indicated in Table 4-2 for the more interesting dates and studied in detail. Unfortunately, MSS data were not recorded in the spring of 1988, and there is a long waiting time for TM prints. For these reasons the procurement decisions for the 1988 data were based solely on the automatic cloud cover assessments.

Table 4-2.   Landsat scene quality and cloud contamination analysis for scenes with less than 30 percent cloud cover (see notes following table).

	Date	Landsat sensors	Path/row	Scene cloud cover (%)	B&W print ordered	Comment
	06/29/88	TM-4	182/24	20	No	Not processed to film
*	05/28/88	TM-4	182/24	0	No	Not processed to film
	01/05/88	TM-4	182/24	20	No	Not processed to film
	10/18/87	TM & MSS	181/24	0	No	Not reviewed
	10/02/87	TM	181/24	10	No	Not processed to film
	09/23/87	TM & MS	182/24	30	Yes	Not processed to film
*	09/07/87	TM & MSS	182/24	20	Yes	Clouds in left quarter; good full scene
	08/22/87	TM	182/24	30	No	Not processed to film
	07/22/87	TM-4	181/24	10	Yes	6.7-in. film available; cloudy
	07/21/87	MSS	182/24	20	Yes	Cloud free near nuclear plant
	06/28/87	TM & MSS	181/24	10	Yes	Clouds to northwest
*	05/11/87	TM & MSS	181/23	10	Yes	Very good; cloud free
	02/04/87	TM & MSS	181/24	0	Yes	Snow cover
	01/10/87	MSS	182/24	0	Yes	Snow cover; ice free cooling pond
	01/03/87	TM	181/24	0	Yes	Cirrus wisps and shadows; poor
	12/25/86	TM	182/24	0	No	No film
	12/18/86	TM	181/24	20	No	No film
	12/09/86	TM & MSS	182/24	10	Yes	Some cirrus and popcorn; poor
*	12/02/86	TM & MSS	181/24	10	Yes	Good
	10/22/86	TM	182/24	20	No	No film
*	10/15/86	TM & MSS	181/24	0	Yes	Good
	09/28/86	MSS	182/24	10	Yes	Popcorn clouds to north
	08/11/86	MSS	182/24	20	Yes	Some cirrus
	08/03/86	TM & MSS	182/24	30	Yes	Clouds to the northwest
	07/18/86	TM	182/24	30	No	No film
	07/03/86	MSS	181/24	10	Yes	Some popcorn clouds

Table 4-2. Landsat scene quality and cloud contamination analysis for scenes with less than 30 percent cloud cover (see notes following table). (Continued)

	Date	Landsat sensors	Path/row	Scene cloud cover (%)	B&W print ordered	Comment
	06/17/86	MSS	181/24	10	Yes	Very good
	06/16/86	TM	182/24	20	Yes	Heavy popcorn
*	05/31/86	TM & MSS	182/24	10	Yes	Very good full scene
*	05/24/86	TM & MSS	181/24	10	Yes	Ok, but some popcorn clouds
	05/16/86	MSS-4	181/24	10	Yes	Good
*	05/08/86	TM & MSS	181/24	0	Yes	Very good
	05/07/86	MSS-4	182/24	0	Yes	Very good
	04/30/86	MSS-4	181/24	10	Yes	Good
*	04/29/86	TM & MSS	182/24	10	Yes	Some popcorn clouds
*	03/21/86	TM & MSS	181/24	0	Yes	Frozen river; ice-free cooling pond
	09/01/85	MSS	182/24	20	No	Cloud to the south
	08/25/85	MSS	181/24	10	No	Cloud free
*	06/06/85	TM & MSS	181/24	0	Yes	Cirrus to the south
	10/25/84	TM & MSS	181/23	10	Yes	Thin cirrus over reactor area
	07/13/84	MSS	181/24	10	No	Very good
	05/01/84	MSS	182/24	20	Yes	Some cloud but good
	06/25/83	MSS	181/24	10	No	Some haze but good

Notes:
1. An * to the left of the date indicates that the data were purchased for that date.
2. Landsat license restrictions apply only to data acquired after 25 September 1985.
3. Only scenes with a cloud cover rating of <30 percent from 1984 to present were reviewed.
4. Not all scenes for 1983 were reviewed.
5. More MSS scenes for 1983 and earlier are available.
6. Unless otherwise specified, all of these scenes are sufficiently free of clouds to do some analysis.

From these observations, we produced a prioritized list of TM imagery (see Table 4-3), and ordered an initial set of imagery (see Table 4-4). This initial set included nine images that spanned the period from 6 June 1985 through 11 May 1987. The two more recent images were ordered later (see Table 4-4) after preliminary results (discussed below) indicated that the area showing stress was still expanding.

Table 4-3. Scene procurement recommendations.

Date	Priority	Sensor	Medium	Area
05/31/86	1	TM	Tape	Full Scene
08/03/86	2	TM	Tape	Quad 4
10/15/86	3	TM	Tape	Quad 3
10/25/84	4	TM	Tape	Quad 3
03/21/86	5	TM	Tape	Quad 3
12/02/86	6	TM	Tape	Quad 3
05/11/87	7	TM	Tape	Quad 3
06/17/86	8	MSS	Tape	Full Scene
02/04/87	9	TM	Tape	Quad 3
05/08/86	10	TM	Tape	Quad 3
06/06/85	11	TM	Tape	Quad 3
04/29/86	12	TM	Tape	Quad 4
08/25/85	13	MSS	Tape	Full Scene
07/13/84	14	MSS	Tape	Full Scene
06/28/87	15	TM	Tape	Quad 3
09/07/87	16	TM	Tape	Full Scene
01/10/87	17	MSS	Tape	Full Scene
05/08/86	18	MSS	Film	Full Scene

Table 4-4. Landsat-scene acquisitions.

Image number	Date	Scene ID	Path/row/quad
1	6/06/85	Y5046208185	181/024/3
2	3/21/86	Y5075008144	181/024/3
3	4/29/86	Y5078908200	182/024/4
4	5/08/86	Y5079808133	181/024/3
5	5/24/86	Y5081408131	181/024/3
6	5/31/86	Y5082108191	182/024/4
7	10/15/86	Y5095808082	181/024/3
8	12/02/86	Y5100608071	181/024/3
9	5/11/87	Y5116608123	181/024/3
10	9/07/87	Y5128508213	182/024/4
11	5/28/88	Y4214308224	182/024/4

Because only a small area was believed to have received a sufficient radiation dose to result in visible stress, only a 1 degree of longitude by 0.5 degree of latitude area was ordered. Table 4-5 shows the corner points of this area area.

Table 4-5. Corner points of the acquired images.

Corner	Longitude ($\pm ddd:mm:ss.s$)	Latitude ($\pm dd:mm:ss.s$)
Upper left	29:45:00.0	51:40:00.0
Upper right	30:45:00.0	51:40:00.0
Lower left	29:45:00.0	51:10:00.0
Lower right	30:45:00.0	51:10:00.0

4.4. IMAGE PREPARATION.

As discussed above, precise registration of images to one another is crucial for change detection. Registration involves three basic processes: ground control point selection, image warping, and resampling. Ground control points (GCPs) are spatial features whose location is known in both images or in one image and a map. The locations of these GCPs are then used to calculate a mathematical mapping (called a warp) from an arbitrary position in one image to the corresponding ground position in the other image or map. This mapping can be envisioned as the stretching and twisting (warping) of one image so that it can be overlaid on the reference image (map). Once overlaid, any position on the ground occurs at the same location in both images. After successful warping, pixels in the warped image will not, in general, be coincident with pixels in the reference image. Instead, they will be off center and skewed relative to those in the reference image. To correct for this problem, the warped image is resampled to a set of pixels congruent with those at the reference image.

The TM data were delivered directly to STX Corporation of Lanham, Maryland, for registration (geocoding). Only the image dated 31 May 1986 was directly registered to maps. The maps used were 1:250,000 scale Joint Operations Graphics (JOGs) identified as Series 1501, Sheet NM 35-3, Edition 2-GSGS and Sheet NM 36-1, Edition 1. The remaining eight images were then registered to the map-registered 31 May 1986 image. This allowed the selection of a greater number of control points, resulting in a more precise registration among the images than could have been attained by registering all of the images to the maps. Two more recently procured images (numbers 10 and 11) were registered in like fashion to the 6 June 1985 image.

Because the maps used to register the first image were Universal Transverse Mercator (UTM) projections, Grid Zone 36, all of the subsequent images were registered to this projection. That is, any of the images can be overlaid on a UTM map (or visa versa). The corner points of the area covered by these images are shown in Table 4-6.

Table 4-6. Corner points of the geocoded images after resampling.

Corner	Longitude (degrees)	Latitude (degrees)	UTM X (meters)	UTM Y (meters)
Upper left	294246.9574E	513956.7881N	272700.	5729000.
Upper right	304459.6821E	514124.8298N	344475.	5729000.
Lower right	304631.7845E	510959.8775N	344475.	5670725.
Lower left	294501.3475E	510833.4597N	272700.	5670725.

16

A 12.8-km sub-area (512 x 512 pixels) was identified for intensive analysis. The corner points of this area are shown in Table 4-7. Unless otherwise specified, these coordinates apply to all color figures shown in this report.

Table 4-7. Corner points (Zone 36 UTM coordinates) of the
512 x 512 pixel area analyzed in this report.

Corner	X (meters)	Y (meters)
Upper left	289900.	5702100.
Upper right	302675.	5702100.
Lower left	289900.	5689325.
Lower right	302675.	5689325.

Figure 4-1 shows a sample image of this 512 x 512 pixel area. The Pripyat river flows through the upper right hand corner of the image. The dark area adjacent to the river is in the cooling pond of the Chernobyl Nuclear Reactor Station. The industrial area comprising the reactor station itself is at the upper left corner of the cooling pond. The cooling water intake channel (right angle bend) and the outlet channel (obtuse angle) are evident. Water circulates counterclockwise in the pond. The reactor buildings are located in an east-west row just above the east-west portion of the intake channel. Reactor four is leftmost in the row.

The city of Pripyat is at the upper center of the image, just south of the river and northwest of the reactor site. The city of Chernobyl, an old river port, is about 10 km to the southeast, not on this image.

The bright green areas in Figure 4-1 are mostly agricultural lands; the bright pinkish or reddish areas are bare fields. The dark green areas are predominantly conifer forests as evidenced by seasonal progressions in subsequent figures.

The standard geometric-correction algorithm applied to TM data (Irons, 1985) results in an image that appears to be somewhat blurred. But, unlike Goldman and coworkers (Goldman, 1987), we made no attempt to sharpen the images. If the images are sharpened, even small (subpixel) registration errors may result in large apparent image-to-image changes for corresponding pixels. Further, because these errors are systematic, real stress at the single pixel level may be entirely obscured by this misregistration-induced apparent stress.
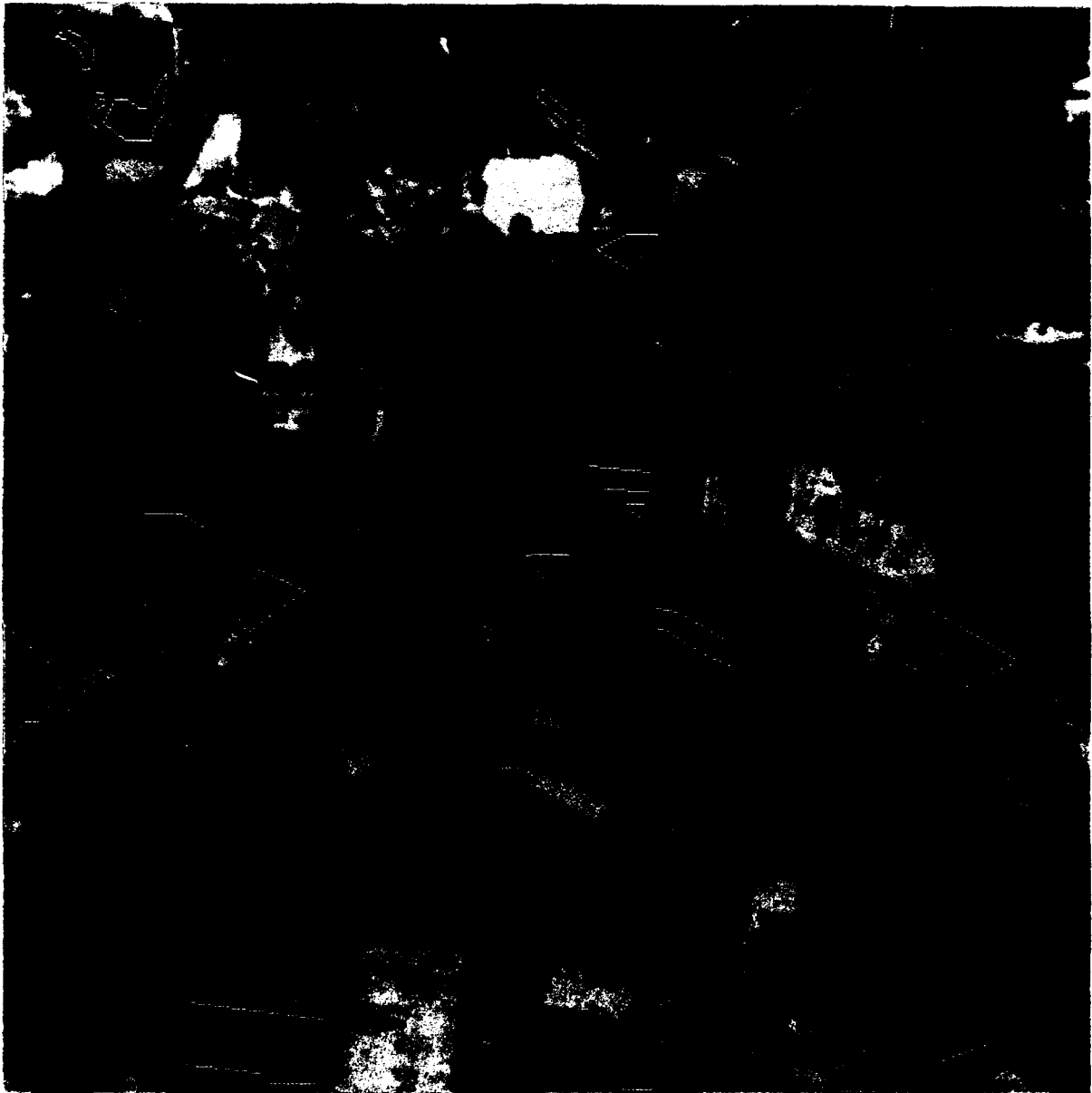
17

Figure 4-1. Vicinity of the Chernobyl Nuclear Reactor Station on 8 May 1986; 7,4,1 false-color presentation (12.8 km by 12.8 km, north is up). Sixteen of the indicated polygons are areas selected as candidate training sets for the forest classification process.

18

SECTION 5

IMAGE ANALYSIS

This section discusses the techniques used to identify forest pixels in the Landsat imagery and reviews the false-color images and forest stress results for each date.

5.1. IMAGE PARTITIONING.

Because only forested areas are of interest for our analysis, we applied methods based on statistical decision theory to eliminate other areas from consideration. Maximum-likelihood classification (Swain, 1978), a parametric method for statistical classification, requires estimates of the parameters of the statistical distributions that are assumed to characterize the variation of spectral intensities over statistically homogeneous regions of the image. The pixels within selected areas of the image (referred to as *training areas* or *training sites)* are appropriately analyzed to estimate statistical parameters of an assumed statistical distribution for the pixels belonging to each class. Each training area yields a set of statistical parameters and a corresponding class distribution in the form of an analytic function involving the class parameters.

The distributions are usually assumed to be multivariate normal in their analytic form. The parameters of the multivariate normal distribution law include the mean vector and the covariance matrix. The mean vector is a band-by-band average of the intensity taken over every pixel in the training site. Thus, if seven bands are used, the mean vector is seven dimensional (i.e., it has seven components, one for each band average). The covariance matrix comprises the covariances estimated from all pairings of the band intensities and will be a square array of dimension equal to the number of bands.

An analytic distribution derived in this way provides a means for estimating the probability that a pixel belonging to the corresponding class will be found to lie at any given point in the multispectral feature space. Thus, probabilities that a pixel belongs to each of the classes under consideration can be estimated at any given point in the multispectral feature space. Maximum-likelihood classification assigns a pixel to the class for which its position in the feature space has the greatest probability. In this manner the pixel classification process assigns each pixel of the image to one or the other of the classes, resulting in a partitioning of the image into the predefined classes.

Training sites are usually determined from ground truth. Unfortunately, because ground truth of the Chernobyl area was not readily available to us at the time of this analysis, we identified training sites visually by spectral characteristics and characteristic texture. Potential training sites identified in this way are displayed as polygons in Figure 4-1.

19

Ideally, assignment of a pixel to a given class depends on the joint probability that it would be characterized by a pixel vector X (its vector of intensity values) while belonging to class ω_i. This joint probability is given by the following equation:

$$p(X, \omega_i) = \frac{p(\omega_i)}{\sqrt{(2\pi)^n |\Sigma_i|}} \exp\left[-\frac{1}{2}(X - M_i)^T \Sigma_i^{-1}(X - M_i) \right] \tag{1}$$

where,

n = the number of bands (also the dimensionality of X and U, and the order of S),

$p(\omega_i)$ = the probability of class ω_i,

M_i = the mean vector for class ω_i,

X = the pixel vector (n intensity values), and

Σ_i = the covariance matrix for class ω_i.

Note that this is *not* a conditional probability. However, it is related to the conditional probabilities by

$$p(X, \omega_i) = p(X|\omega_i) \, p(\omega_i) = p(\omega_i|X) \, p(X) \, . \tag{2}$$

The pixel is then assigned to class ω_i if and only if

$$p(X|\omega_i) \, p(\omega_i) \geq p(X|\omega_j) \, p(\omega_j) \tag{3}$$

for all j = 1,2,. . ., m, where m is the number of classes. Because in this study the class probabilities $p(\omega_i)$ were unknown, they were assumed to equal one another, causing the class assignments to be determined by the conditioned probability of the pixel vector's occurrence, given the hypothetical class.

For this study we required the training sites to be minimal in number and near the reactor, but not subject to radiation stress. We chose the smallest possible number of training sites for the analysis because maximum-likelihood classification is computationally expensive. Ideally, one training site would be selected for each distinguishable forest type. The distinctions among forest types might be based on ground truth data such as differences in the mixture of coniferous and deciduous trees, age of the stand, densities or crown closures, or species in the area. Because little ground truth was available at the time of the study, the selection of training sites had to be based entirely on their remotely sensed multispectral characteristics. It was found that two training sites

20

provide a satisfactory classification of the pixels in the image, a classification that includes nearly all of the pixels in regions believed to be forested while including few in regions that were clearly not forested. In the process of selecting these two training sites a number of potential training sites were selected in the area near the Chernobyl nuclear reactor; these are shown on Figure 4-1. Note that only 16 of these are forest. Five were chosen to include only water, and one was believed to be sand. These nonforest sites were chosen in anticipation of a need to normalize the various images using features whose spectral response could be assumed stable over time. Because the method finally chosen to detect stress did not require such normalization, the nonforest training sites were not used.

Partitioning the image assigned every pixel in the image to one or the other of the predefined classes. Because we were interested only in forests, we selected only forest training sites and included only forest classes in the set of predefined classes. After the image was partitioned in this way, pixels that obviously contained water, bare soil, and all manner of other things were assigned, along with the forest pixels, to the closest of the forest classes. As yet no consideration had been given to the possibility that a pixel's spectral features might have been far more likely to have arisen among pixels belonging to nonforest classes such as water, bare soil, etc; we had yet to define what was and was not a forest.

Nonforested areas could have been removed from consideration by maximum-likelihood classification in the same manner as was used for the forest classes. However, this would have entailed developing training areas or sites for every class of landcover that occurred in the image, and it would have required that the a probability be calculated for every pixel for every such class. A computationally more efficient process was to apply a threshold to the probability computed for a pixel's membership in the forest classes. If the pixel's multispectral features occurred in a particular forest class with a probability less than a certain threshold value, the pixel was assumed to belong to a class other than that forest class. In practice, we adjusted the probability threshold while monitoring the outcome of the classification process, raising the threshold if too many stray pixels in the image seemed to be assigned to the desired classes and lowering the threshold if too many of the pixels thought to belong to the desired classes were being rejected. The resulting statistical decision process may be looked upon as a casual implementation of the Neyman-Pearson decision rules; the threshold for pixels belonging to the forest class was made as low as possible without accepting too many pixels that lay outside the apparent areas of forest.

When the image was partitioned using only one training site (e.g., training site 4 on Figure 4-1), many of the forested areas were misclassified as nonforested areas (errors of omission) when a reasonable threshold value was selected. This threshold value was determined qualitatively by viewing the effect of a given threshold value on the classification. Lowering the

threshold sufficiently would include all suspected forested areas, but at the cost of including too many other areas that were perceived to be nonforested (errors of commission).

Finding that no adjustment of the threshold would lead to an entirely satisfactory result, we concluded that the use of only one training site was not sufficient and considered using two. The question then became "which two?" As discussed above, the selection should be based on statistical arguments. To this end, PSR developed a modified form of the transformed divergence (Swain, 1978) specifically for use in this study. The divergence between two training sites was defined by

$$D_{ij} = \frac{1}{2} \, tr\left[\left(\Sigma_i - \Sigma_j\right)\left(\Sigma_j^{-1} - \Sigma_i^{-1}\right)\right] + \frac{1}{2} \, tr\left[\left(M_i - M_j\right)\left(\Sigma_i^{-1} + \Sigma_j^{-1}\right)\left(M_i - M_j\right)\right] \quad (4)$$

The transformed divergence is given by

$$D_{ij}^T = 100\left[1 - exp\left(\frac{-D_{ij}}{8}\right)\right]. \quad (5)$$

Unfortunately, the transformed divergence saturated (yielded 100) for even small differences in cluster statistics if a large number (>4) of bands was used. In addition, the results were strongly dependent on the number of bands used. To reduce the effects of these problems, we defined the modified transformed divergence by

$$D_{ij}^{MT} = 100\left[1 - exp\left(\frac{-D_{ij}}{2n}\right)\right]. \quad (6)$$

The modified transformed divergence was relatively independent of the number of bands used in the analysis provided that the bands used were not highly correlated. Table 5-1 presents the modified transformed divergence between every pair of potential forest training sites shown in Figure 4-1. These results led us to choose sites 3 and 4 as training sites to partition the 6 June 1985 image. Figure 5-1 shows the results of this classification. Areas colored green were assigned to the class developed from training site 4, and areas colored yellow, to the class developed from training site 3. This classification map (recall that the image is registered, so this really is a map) was then overlaid on a gray-scale TM band 4 image of the area. It is not important for the present analysis to know the difference between the types of forest in these training sites. We need only to account for their statistically distinct multispectral characteristics.

Table 5-1. Training site modified transformed divergencies.

	1	2	3	4	5	6	7	8	9	10	11	12	13	14	15	16
1	0.0	15.2	35.2	87.9	41.3	27.1	46.4	89.8	62.4	28.1	38.7	89.8	93.5	52.8	90.1	38.1
2	15.2	0.0	32.6	99.7	63.7	51.7	66.9	98.6	57.9	52.2	70.3	95.5	93.8	82.6	99.3	37.2
3	35.2	32.6	0.0	100.0	84.2	74.6	86.6	99.8	77.2	64.4	79.5	99.5	98.5	92.8	99.8	68.8
4	87.9	99.7	100.0	0.0	88.2	90.6	96.4	74.4	100.0	98.2	78.0	64.2	95.6	55.5	54.0	99.9
5	41.3	63.7	84.2	88.2	0.0	41.4	18.2	46.3	87.8	52.9	52.3	66.4	75.8	76.1	63.0	48.4
6	27.1	51.7	74.6	90.6	41.4	0.0	55.4	87.0	65.6	30.2	19.4	79.9	87.5	46.6	83.3	43.3
7	46.4	66.9	86.6	96.4	18.2	55.4	0.0	59.9	86.7	49.1	54.6	76.2	84.3	84.3	86.9	45.1
8	89.8	98.6	99.8	74.4	46.3	87.0	59.9	0.0	100.0	89.3	80.2	78.7	87.7	85.5	33.2	97.0
9	62.4	57.9	77.2	100.0	87.8	65.6	86.7	100.0	0.0	59.4	74.1	99.6	99.2	96.8	100.0	34.4
10	28.1	52.2	64.4	98.2	52.9	30.2	49.1	89.3	59.4	0.0	21.2	96.5	98.2	82.1	88.5	31.8
11	38.7	70.3	79.5	78.0	52.3	19.4	54.6	80.2	74.1	21.2	0.0	88.3	94.8	66.2	74.2	54.0
12	89.8	95.5	99.5	64.2	66.4	79.9	76.2	78.7	99.6	96.5	88.3	0.0	49.4	71.4	88.5	94.3
13	93.5	93.8	98.5	95.6	75.8	87.5	84.3	87.7	99.2	98.2	94.8	49.4	0.0	90.5	92.9	93.4
14	52.8	82.6	92.8	55.5	76.1	46.6	84.3	85.5	96.8	82.1	66.2	71.4	90.5	0.0	74.7	91.1
15	90.1	99.3	99.8	54.0	63.0	83.3	86.9	33.2	100.0	88.5	74.2	88.5	92.9	74.7	0.0	99.2
16	38.1	37.2	68.8	99.9	48.4	43.3	45.1	97.0	34.4	31.8	54.0	94.3	93.4	91.1	99.2	0.0

Figure 5-1.   Partitioning of 6 June 1985 image into classes derived from training sites 3 (yellow) and 4 (green). Gray-scale background consists of nonforested areas.

To minimize the effect of local atmospheric variations, we wished to choose training sites as close to the reactor as possible. On the other hand, if training sites too close to the reactor were chosen, they could have been subject to radiation stress, especially if the image used to identify forested areas was acquired after the accident. This study used the image dated 6 June 1985 (before the accident) to partition the image. Nevertheless, the training sites were selected to be outside the area in which radiation stress was expected to appear in postaccident images.

5.2. MAPPING STRESS.

In this section, each of the selected images is reviewed in chronological order with important features identified. These require some explanation. Standard false-color prints of TM data display band 4 as red (R), band 3 as green (G), and band 2 as blue (B).

This presentation is referred to as a 4,3,2 RGB false color. In this report, the color ordering will always be RGB unless otherwise stated). As discussed in Section 2 above, vegetation should appear red in this standard presentation. The shadowing of trees by one another causes forests to appear highly textured and darker.

There is another standard false-color display gaining acceptance in the community (Johnson): the 7,4,2 false color. This results in a more appealing and less arcane image because it appears much like a normal (3,2,1 RGB), true-color image but has better contrast information content; the 7,4,2 false-color image contains information from three quite different regions of the spectrum, rather than being restricted to the visible region as is a 3,2,1 image. In the 7,4,2 presentation bare soils tend to appear red, with drier soils appearing a brighter red color. Vegetation appears green, and shallow or turbid water tends to appear blue.

The color prints presented here use a nonstandard 7,4,1 false-color display. This combination captures most of the advantages of the standard 7,4,2 false-color display, but with the added advantage that it makes cirrus clouds more obvious. Because cirrus clouds can (and invariably do) interfere with analysis, knowledge of the location of even light cirrus clouds can be important.

For images acquired on or after 29 April 1986, stress maps have been produced using PSR's Hyperscout change detection algorithm with the 6 June 1985 image as reference. The stress algorithm assigns a single number, called the *stress index*, to each forested pixel in the image, and these are displayed in the stress map. Again, the resulting stress map, like the images from which it was derived, is registered to the UTM projection, Grid Zone 36. The stress map could be displayed as a gray scale, but the resulting image would be difficult to discern in areas manifesting low stress. In this report, the stress gray scale is converted to a color scale. A legend showing this color scale appears with the stress maps shown below. Values of the highest stress index are colored red. As the stress index decreases, the color shifts continuously through orange, yellow, green, and blue to magenta. Thus, magenta-colored areas are the least stressed. Nonforested

25

areas, which could not be analyzed for stress, are filled in with a gray-scale TM band 4 image to establish a spatial context for the interpretation. The accompanying text discusses significant features of these stress maps, as well as of the 7,4,1 false-color images.

The stress maps derive from an analysis of only three of the 7 bands, namely, 3, 4, and 7. Band 6 (the thermal band) was not used because the images frequently included clouds. The low temperature of clouds, coupled with the 120-m resolution of band 6, affects an area larger than that where clouds are evident. Even light cirrus clouds would mislead a stress calculation that includes band 6 because of its high sensitivity to the temperature of the cloud cover. Bands 1 and 2 (blue and green) were not used because they also are relatively sensitive to cirrus clouds and atmospheric scattering as compared to the red or infrared. This left only bands 3, 4, 5, and 7. Bands 5 and 7 are very highly correlated, so either may be used. We arbitrarily choose band 7 over band 5.

Figure 5-2 shows the reference image from 6 June 1985, 1 year before the accident. Recall that this is also the image used to classify forest types. A significant feature of this image is that the forested areas due west of the reactor appear darker and may even have a brownish tint. This is also the type of coloring (spectral reflectance) that might be expected from radiation-stressed coniferous forests. Because it is unlikely that the coloring present on 6 June 1985 was caused by radiation stress (certainly not that caused by the release on 26 April 1986), this image indicates that qualitative (visual) identification of stress from the false-color images can be misleading.

Figure 5-3 shows the 21 March 1986 image also taken before the accident. Some snow cover was evident (blue color), and the rivers (but not the warm cooling pond) were ice covered. At training site 3 very little snow cover was visible through the canopy. On the other hand, some snow appeared at training site 4. This observation can be interpreted in at least two ways. First, training site 4 may have more deciduous trees, or, second, the forest may not be as dense in training site 4 as it is in training site 3. Which, if either, of these interpretations is correct has not been determined.

A study, similar in intent to this study, was recently preformed by Goldman and coworkers (Goldman, 1987). They used enhanced Landsat TM data to identify stress visually. They concluded that stress could not be detected visually on images taken before 16 June 1986 (i.e., until *more than 7 weeks after the accident*).

Three days after the accident, Landsat acquired an image of the reactor area. This image, taken 29 April 1986, shows some cloud cover as seen in Figure 5-4. The reactor, still extremely hot, was readily apparent as a deep red area due north of the reactor water inlet pool. Another reddish white feature appeared 1.1 km to the west of the reactor and was mistakenly reported to be another burning reactor. There was no visibly stressed vegetation.

Figure 5-2.   Date: 6 June 1985, 1 year preaccident; 7,4,1 false color. This date was used as
               a reference for change detection.

27

Figure 5-3. Date: 21 March 1986, 2 months preaccident; 7,4,1 false color. Snow cover is evident (bright blue) around the forest patches.

Figure 5-4. Date: 29 April 1986, 3 days postaccident; 7,4,1 false color. The deep red pixel is the thermal emission from the hot reactor core.

Figure 5-5 presents the stress map for this date. The area of high stress index that appears 4 km due west of the reactor was cleared before the accident. Nearly all of the rest of the apparent stress was caused by clouds. The centers of cumulus clouds and their shadows usually appear deep red in the stress index maps, while at their fringes there appears a sharp, rainbowlike progression of colors from deep red to magenta. Cirrus clouds are much more insidious; their effects vary in color and extent. In some cases cirrus clouds show no effect at all, while in others, they produce a pattern of apparent stress similar to that expected of real stress. In Figure 5-5, there is a small area approximately 0.9 km west by southwest of the reactor that has a sufficiently high stress index to be displayed in the green to yellow color range. On the basis of this single image, it is debatable whether this is real stress, cloud effects, smoke, debris covering the foliage, or something else. A qualitative measure of the statistical nature of the noise can be obtained by looking at areas that were not stressed (e.g., training site 3). These areas are colored mostly blue and magenta except near the edges of the forests. From this observation, we conclude that areas in the stress map speckled blue and magenta are probably not really stressed but only the effect of random noise-level detections of change. In addition, any apparent stress that appears only at the edges of forests is suspect, because of possible registration errors.

The 8 May 1986 image, presented in Figure 5-6, was collected 12 days after the accident. There were no clouds in the image, nor was there stressed foliage visible in the 7,4,1 false-color presentation.

Figure 5-7 presents the stress map made from the 8 May 1986 image. In it appears a very well defined 0.9-km long strip of forest, beginning 2 km west by southwest of the reactor and running to the west, where stress was apparent. This area also had a higher than normal stress index on 29 April 1986, but the area was not as clearly defined. The shape of this stressed area was consistent with that of a directed explosion or wind-deposited fallout. Because by this time the fire at the reactor was reported to have been extinguished, the detected change seems unlikely to be attributable to smoke. Thus, in this stress map we can very clearly see *some indications of accident-related stress or change that appeared within 12 days after the accident.* Located 6 km south of the reactor there appears an apparent stress or change feature that we have interpreted to be an artifact of the change analysis algorithm. The exact cause is unknown. This artifact appears on almost all of the images that follow; its stress index changes very little in time.

Figure 5-5. Date: 29 April 1986, 3 days postaccident, forest stress map. colored according to indicated scale. Gray-scale background consists of nonforested areas.

Figure 5-6. Date: 8 May 1986, 12 days postaccident; 7,4,1 false color.

Figure 5-7. Date: 8 May 1986, 12 days postaccident, forest stress map.

Figure 5-8 shows the 24 May 1986 image collected 4 weeks after the accident. Although it is difficult to see on the 7,4,1 false-color image, there was a large cirrus cloud in the area of the reactor. There were also some "popcorn" clouds in the area. The obscuration of the cirrus cloud and the natural color of the area make positive visual detection of stress uncertain in the false-color image. On the other hand, an area of change becomes very obvious and spatially well defined when presented on the corresponding stress map (Figure 5-9). Unfortunately, so does the large cirrus cloud. The cirrus cloud appears as a blue to green swath on the stress map, affecting the bulk of the eastern side of the image. The "popcorn" clouds and their shadows show up as deep red. By 24 May 1986 aerial spraying to prevent the wind from redistributing radioactive dust, along with the dust itself, may have contributed to the changes that were detected.

The image taken on 31 May 1986 (Figure 5-10) also included some clouds. Positive visual identification of stress remains uncertain, but the stress map shows the stressed area very clearly (Figure 5-11). Little change appears in the spatial distribution of stress between 24 and 31 May, except that a small new area just south of the previously stressed area began to indicate a very high stress index. Because this new area was adjacent to a road, it probably indicates changes caused by human activities other than radiation release.

After 31 May 1986, the next image selected for analysis was that collected 15 October 1986. An interim image collected 16 June 1986 was not purchased because of cloud cover exceeding our standards.

By 15 October 1986 a band of stressed forests that appeared to the west of the reactor can be readily discerned in the false-color image (Figure 5-12). Also visible is evidence of extensive human activity. The Soviets had started to clear some of the contaminated forests near the road that passes to the west of the reactor. There was evidence of extensive diking operations in the northwest and northeast corners of the image. Indications appeared of a cleared swath passing through the coniferous forest to the southwest of the reactor. Because this image was collected in the fall and there were deciduous trees in the area, the spectral definition of stress becomes affected by the natural changes of the deciduous foliage and the seasonal sun angle changes. As a result, the apparent stress is lower than before. Examination of the stress map in Figure 5-13 confirms this hypothesis. The stressed area remains obvious and fairly well defined, but the stress index is lower.

The situation regarding deciduous foliage is similar on 2 December 1986 (Figure 5-14). In addition, the low sun elevation causes a further loss of sensitivity. Although the stresses (Figure 5-15) appear lower than before, the areal extent of the stress does not appear to have changed significantly.

34

Figure 5-8. Date: 24 May 1986, 4 weeks postaccident; 7,4,1 false color.

0   128   256

Stress Index

Figure 5-9. Date: 24 May 1986, 4 weeks postaccident, forest stress map.

Figure 5-10. Date: 31 May 1986, 5 weeks postaccident; 7,4,1 false color.

0   128   256

Stress Index
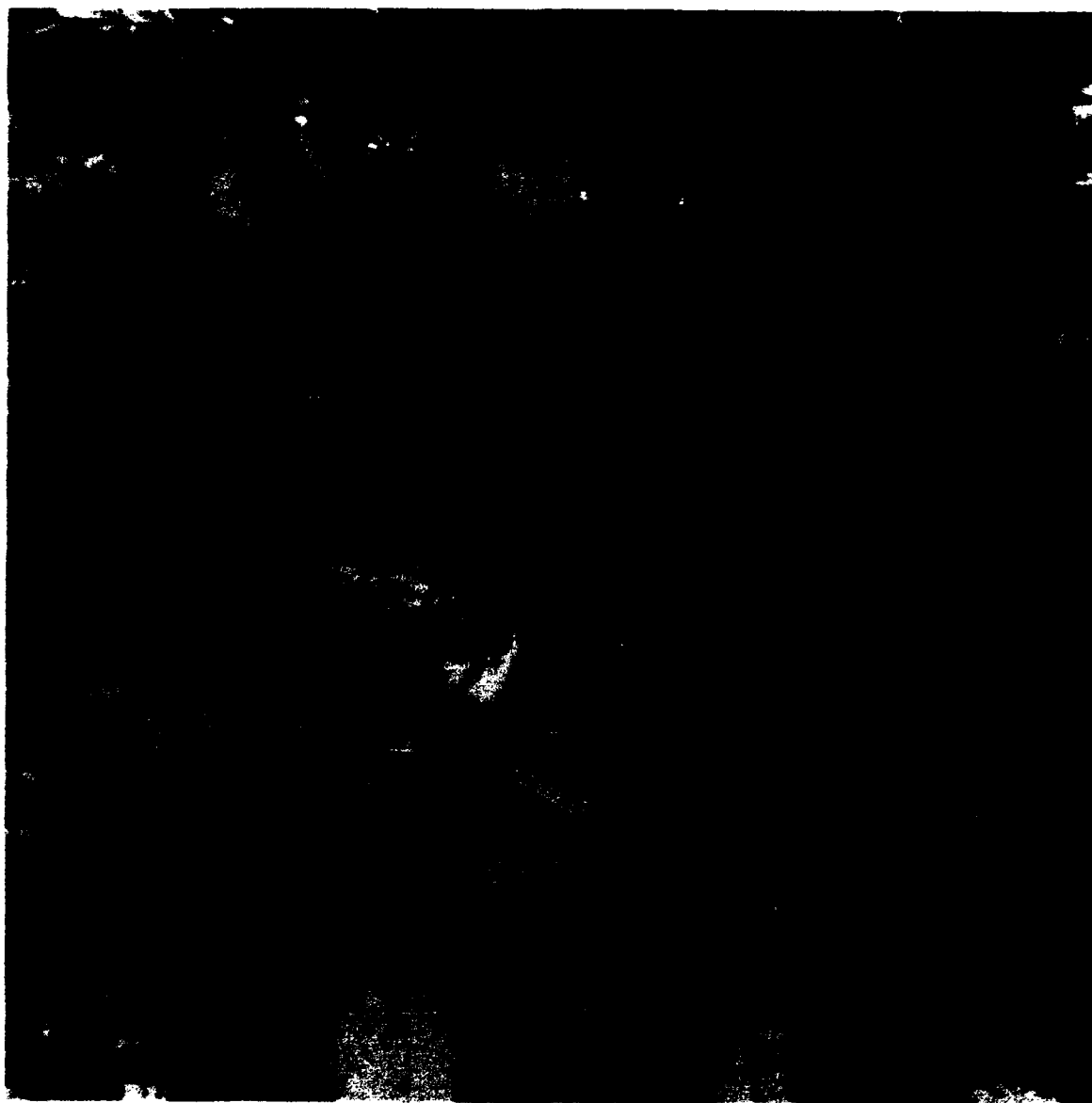
Figure 5-11. Date: 31 May 1986, 5 weeks postaccident, forest stress map.
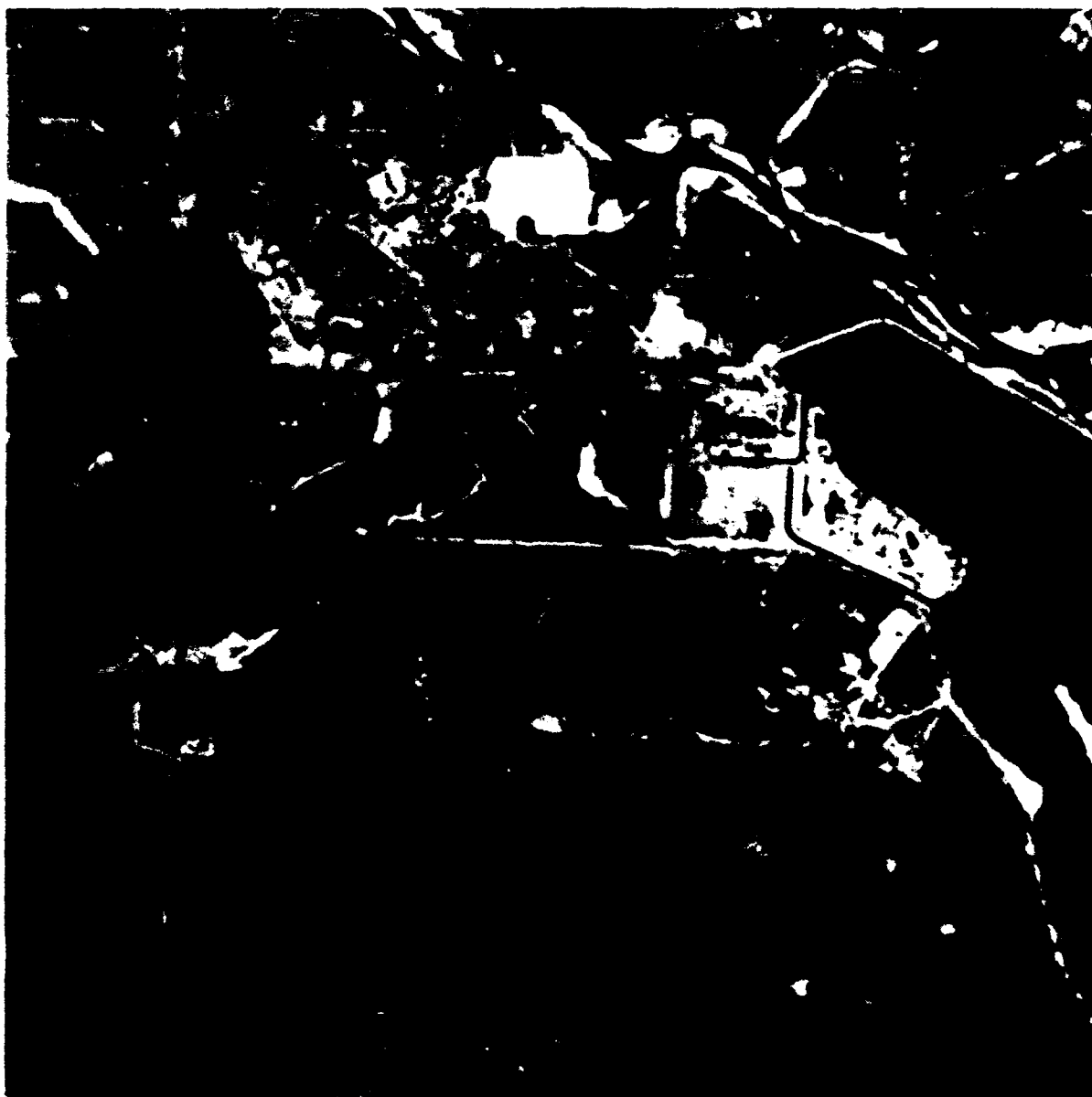
Figure 5-12. Date: 15 October 1986, 5.6 months postaccident; 7,4,1 false color.

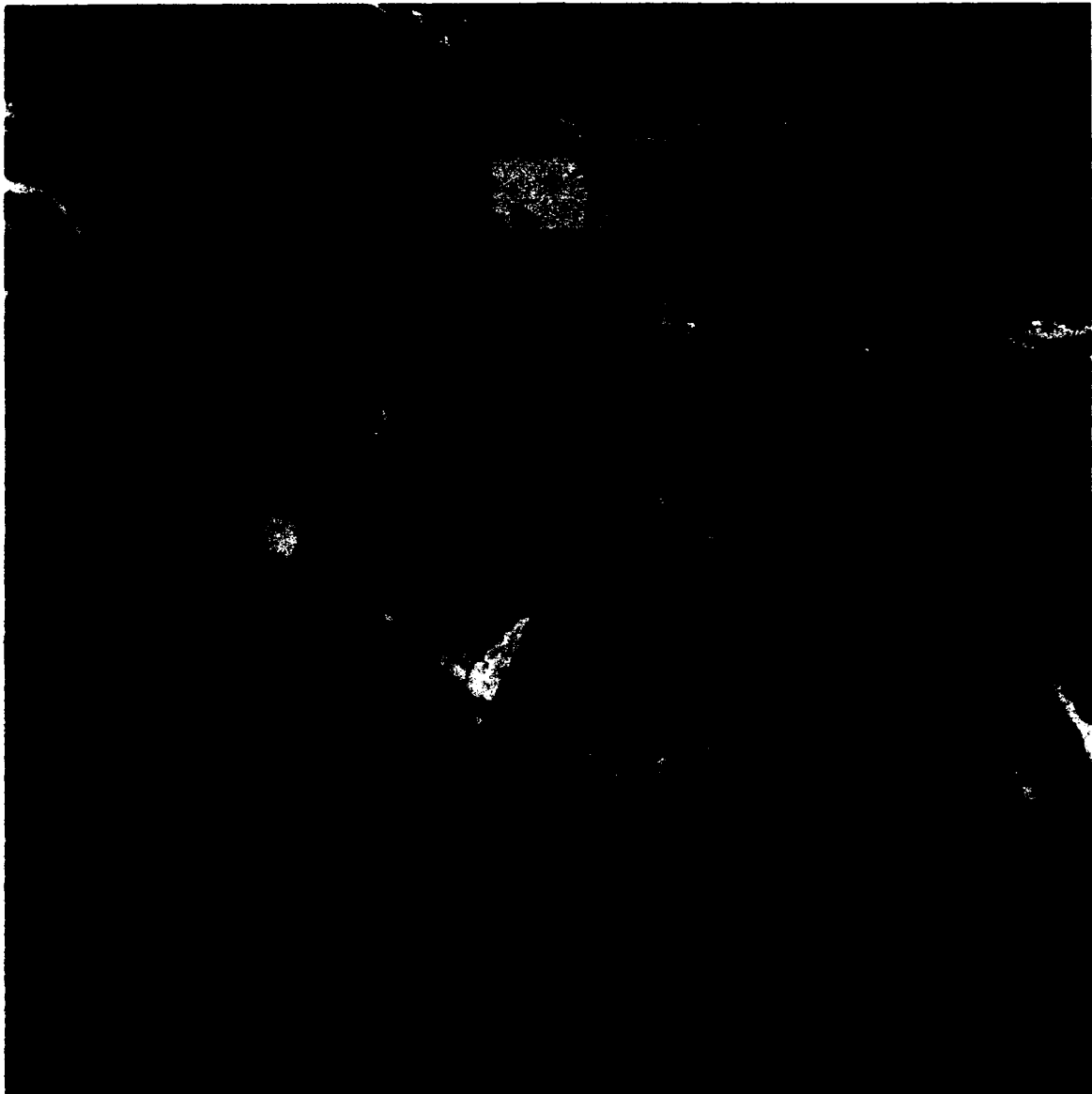0   128   256

Stress Index

Figure 5-13. Date: 15 October 1986, 5.6 months postaccident, forest stress map.

Figure 5-14. Date: 2 December 1986, 7.2 months postaccident; 7,4,1 false color.

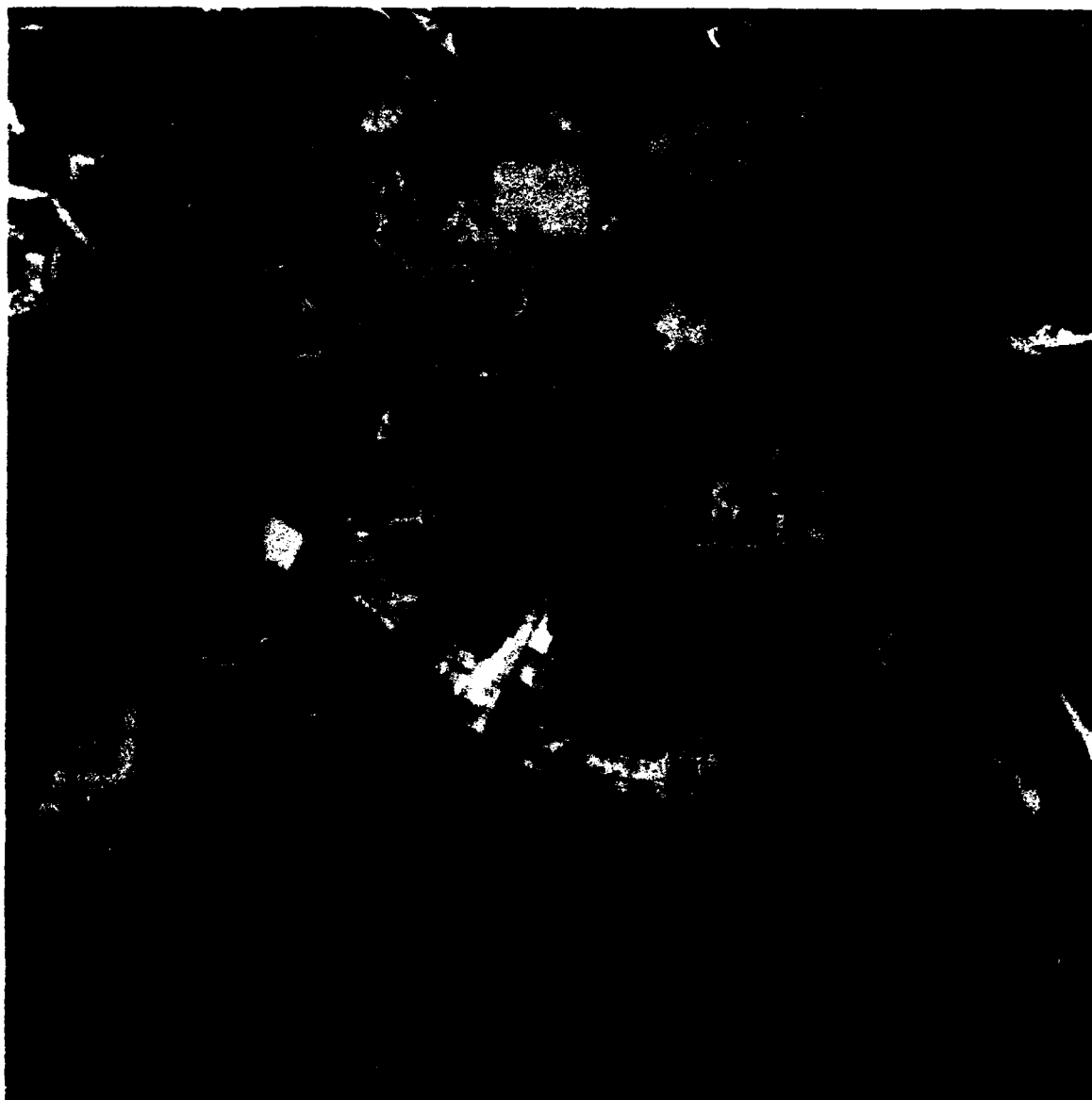|		
0	128	256

Stress Index

Figure 5-15. Date: 2 December 1986, 7.2 months postaccident, forest stress map.

The Soviet mitigation efforts were much more extensive by 11 May 1987 (Figure 5-16). A large area is cleared to the west of the reactor complex, as is an even larger area south by southeast of the reactor. Much of the diking appears to have been completed, and the areas behind the dikes appear flooded. Again, there is a rather large cirrus cloud partially obscuring most of the forests in the western part of the image.

Goldman and coworkers (Goldman, 1987) state that no new stressed areas had appeared by 11 May 1987. Indeed, a visual inspection of the false-color image provides no evidence to the contrary. However, the stress map indicates significant new areas beginning to show stress. Before looking at the stress map, the reader may find it enlightening to attempt to identify these areas visually in the false-color image. As an aid to the reader, Figure 5-17 shows Soviet-supplied gamma dose rate contours dated 1 May 1987 overlaid on the TM image. This ground truth will be discussed in detail in Section 6 below. The innermost contour is for 100 mR/hr, with contours for 50, 10, 5, 2, 1, 0.5, and 0.1 mR/hr appearing progressively outward. If these contours are correct, the bulk of the coniferous forest to the south was still receiving a dose of at least 5 mR/hr, and all areas between the coniferous forest and the cooling pond to the east and the reactor complex to the north were receiving a dose of at least 10mR/hr. Because the areas receiving doses higher than this had already shown an elevated stress index, these areas were the most likely next candidates.

Turning to the stress map shown in Figure 5-18a, we see that these areas were indeed beginning to show symptoms of stress. These newly stressed areas included much of the coniferous forest to the south of the reactor and nearly all of the forested areas between the coniferous forest and the cooling pond to the east and the reactor complex to the north. For ease of comparison, Figure 5-18b shows the dose rate contours overlaid on the stress map from Figure 5-18a.

No images that were free of clouds and haze (see Table 4-2) were collected in 1987 after 22 July 1987. However, an image taken 7 September 1987 (Figure 5-19) was procured to help confirm the indications of continued stress implied by the 11 May 1987 stress map. Unfortunately for the comparison, the Soviets had cleared much of the suspect area lying within the 10 mR/hr dose contour. The northeastern edge of the coniferous forest continued to appear heavily stressed (Figure 5-20) but not as heavily stressed as before. The apparent reduction in stress may have been due to the heavy haze. Indications of new stress appear in the 7 September 1987 stress map in an area just north of the area first showing stress.

Figure 5-16. Date: 11 May 1987, 1 year postaccident; 7,4,1 false color.

Figure 5-17.   Soviet-supplied gamma dose rate contours of 1 May 1987 overlaid on the
11 May 1987 7,4,1 false-color image. The innermost contour is 100 mR/h, the
next innermost 50 mR/h, then 10, 5, 2, 1, 0.5 and 0.1 mR/h, respectively.

45

0   128   256
Stress Index
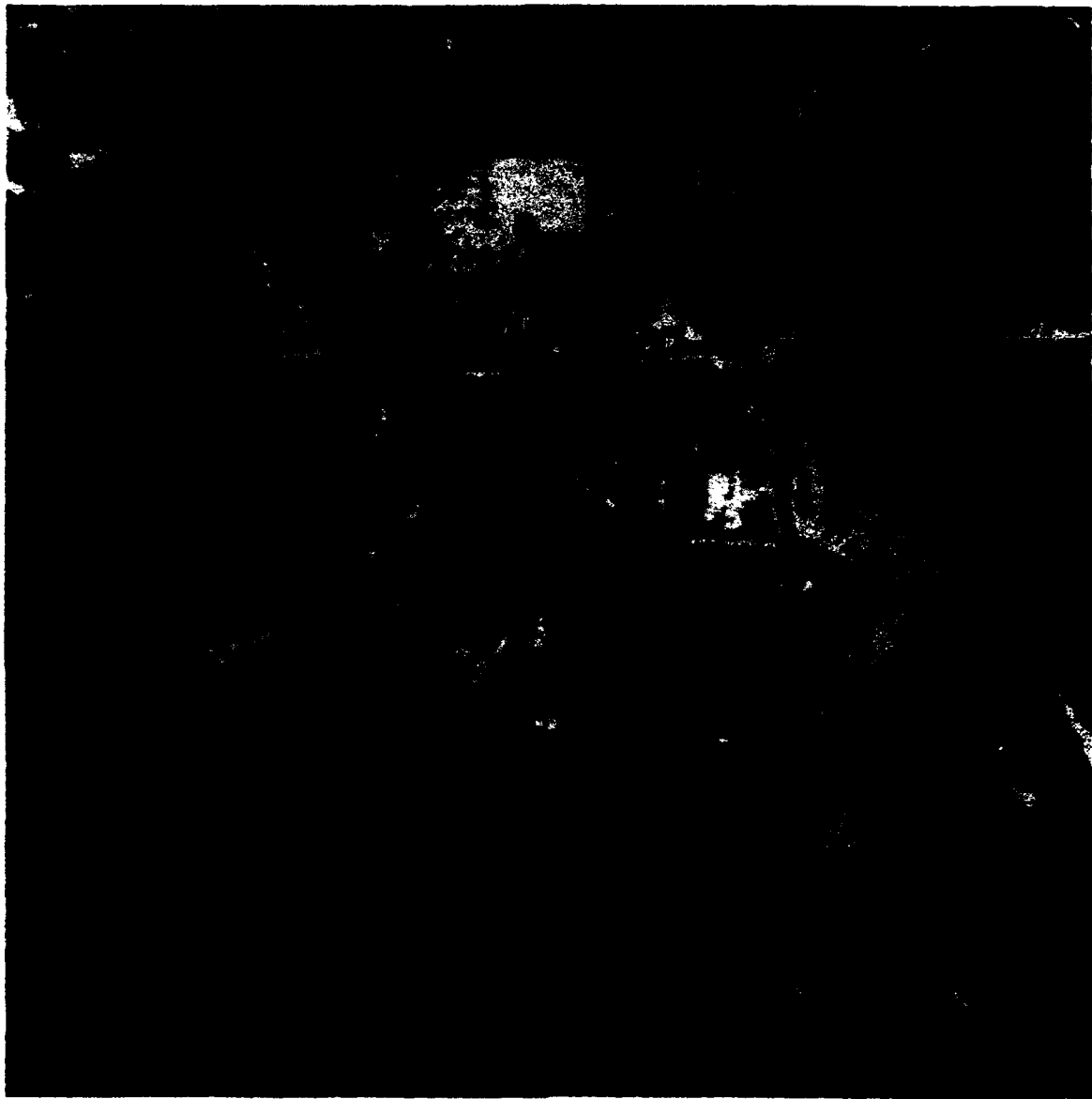
Figure 5-18a. Date: 11 May 1987, 1 year postaccident, forest stress map.

0   128   256

Stress Index
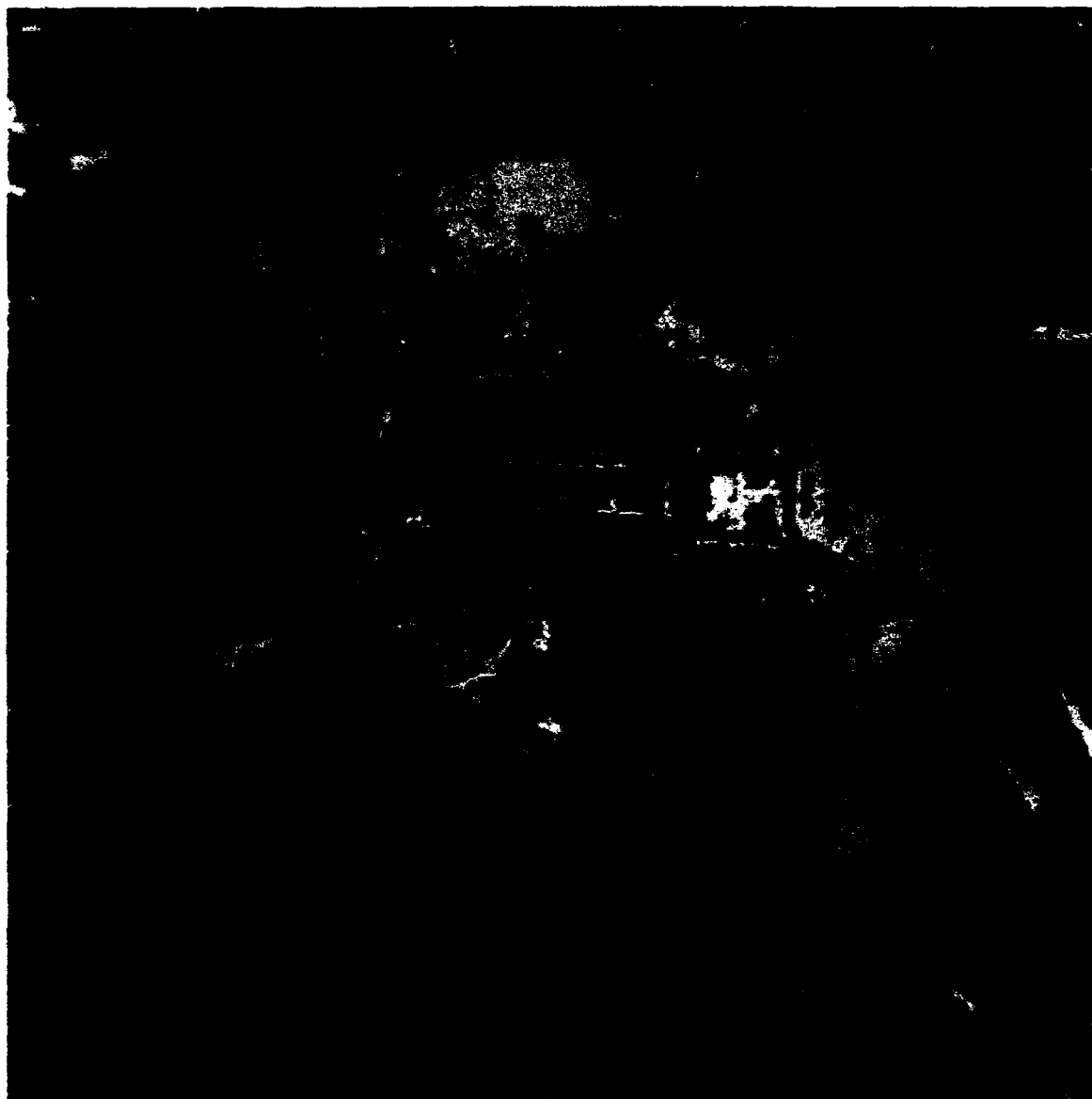
Figure 5-18b.   Date: 11 May 1987, forest stress map with gamma dose rate contours of 1 May 1987 (see Figure 5-17 for contour values).

Figure 5-19. Date: 7 September 1987, 16 months postaccident; 7,4,1 false color.

0   128   256

Stress Index
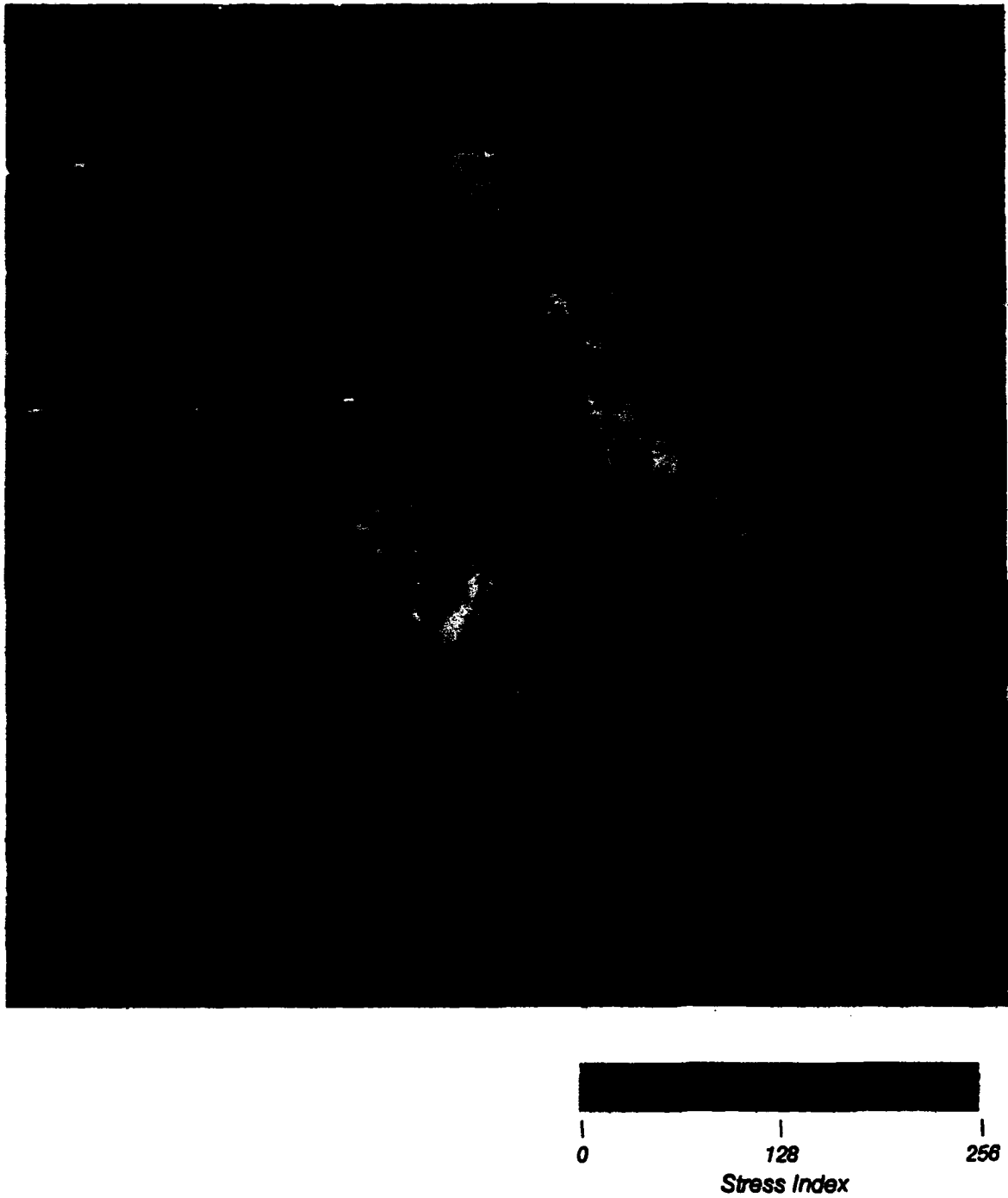
Figure 5-20. Date: 7 September 1986, 16 months postaccident, forest stress map.

Because newly stressed areas were still being found and the 7 September 1987 image was of low quality, a more recent image was procured. This image, dated 28 May 1988, is presented on Figure 5-21. Again, Soviet mitigation efforts had cleared some of the newly suspect areas, so continued monitoring of those areas was not possible. The clearing of the newly suspect areas suggests that these areas had been affected enough that they needed to be decontaminated, although no mitigation efforts were applied to the coniferous forest to the south of the reactor, at which signs of stress persisted (Figure 5-22).

Figure 5-21. Date: 28 May 1988, 25 months postaccident; 7,4,1 false color.

51
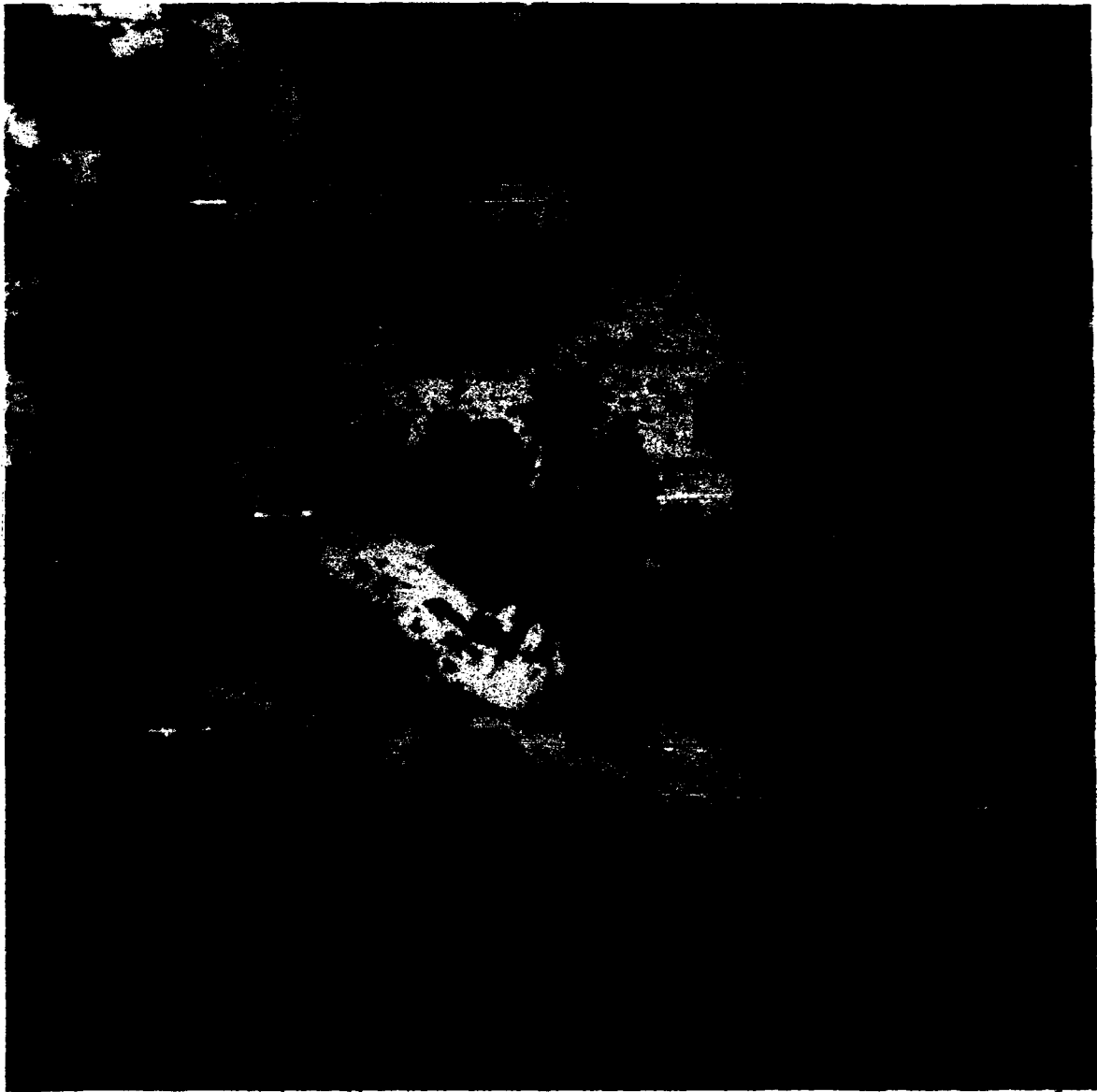
Figure 5-22. Date: 28 May 1988, 25 months postaccident, forest stress map.

SECTION 6

GROUND TRUTH

Some ground truth became available (Asmolov, 1987) in the form of gamma radiation dose contours for 1 May 1987 (i.e. approximately 1 year after the accident). Unfortunately, there are a number of difficulties associated with the use of these data. First, the copy of the dose contours that was available to us is very poor; the contours appear to be hand drawn, and in some places the contours are not closed, making digitization difficult. Also, the contour map has no grid lines and no accurate ground control points (GCPs). In fact, the only usable GCPs are river bends. Further, the indicated courses of these rivers on the contour map do not match the maps that were used to register the images. Because they match the images fairly well, registration directly to the images is a viable alternative. Two cities are shown as circles, but the location of one of them, Chernobyl, is apparently in error by several kilometers. The course of the river Uzh also appears to be in error near this city. The location of the reactor itself is not marked on the map.

In spite of these difficulties, 36 GCPs were identified. Using these GCPs, the coefficients of a second-order warp were calculated by means of a least squares algorithm. When this warp was applied to the digitized contours and the results overlaid on an image, the 100 mR/h contour was centered on reactor 3 instead of reactor 4. Use of a third-order warp resulted in unacceptable (i.e., unlikely) distortions of the contours near the edges of the map. Attempts to generate a fourth-order warp were unsuccessful. Because the ability to weigh GCPs preferentially is inherent to the algorithm used, another GCP, the best guess of the location of the reactor based on the shape of the contours, was added to the set and given a relative weight of 100. The coefficients for a second-order warp were then recalculated using the least squares algorithm. The equations of this warp are shown in equations 7 and 8:

$$x_{ref} = a_1 + a_2 \cdot x + a_3 \cdot y + a_4 \cdot x^2 + a_5 \cdot x \cdot y + a_6 \cdot y^2 \tag{7}$$

and

$$y_{ref} = b_1 + b_2 \cdot x + b_3 \cdot y + b_4 \cdot x^2 + b_5 \cdot x \cdot y + b_6 \cdot y^2 \tag{8}$$

where,

a_i = the coefficients of the warp for the x-coordinate of the image,

b_i = the coefficients of the warp for the y-coordinate of the image,

x = the x-coordinate of a point on the dose contour map,

x_{ref} = the corresponding column (x-coordinate) on the image, which is related to UTM map coordinates,

y = the y-coordinate of a point on the dose contour map, and

y_{ref} = the corresponding row (y-coordinate) on the image, which is related to UTM map coordinates.

The x- and y-axes of the contour plots are arbitrary because no grid lines or map projection was given for the dose contour map. Still, the relative magnitudes of these coefficients are of some interest; they are presented in Table 6-1. A measure of the accuracy of the registration can be obtained by warping the location of the GCPs on the contour map through Equations (7) and (8); then comparing these warped coordinates to the true location of those GCPs in the image. These results are presented in Table 6-2. The contour lines were warped and overlaid on an image (Figure 5-17). In order starting with the innermost, the contours are for doses of 100, 50, 10, 5, 2, 1, 0.5 and 0.1 mR/h.

Table 6-1. Second order warp coefficients for the gamma dose contours.

i	a_i	b_i
1	-0.2760500E+04	0.4388116E+04
2	0.1866979E+00	0.1391407E+00
3	-0.4149658E+00	-0.4166605E+00
4	0.8310569E-05	-0.3711088E-05
5	0.1337978E-04	-0.1319325E-05
6	0.1379850E-04	-0.5189849E-05

Table 6-2. Accuracy of the registration of GCPs.

x	x_{ref} (pixels)	x_{fit} (pixels)	Error (pixels)
14864.79	1024.00	1024.99	0.99
13347.76	249.00	271.18	22.18
13376.74	271.00	282.24	11.24
13525.32	365.00	357.72	-7.28
13434.05	297.00	301.57	4.57
13533.28	364.00	352.89	-11.11
13620.08	397.00	387.50	-9.50
13750.20	470.00	459.64	-10.36
13847.89	505.00	504.52	-0.48
13866.87	509.00	511.20	2.20
14116.60	653.00	648.12	-4.88
14083.66	635.00	619.49	-15.51
14224.67	712.00	700.87	-11.13
14381.22	794.00	775.78	-18.22
14688.25	939.00	936.75	-2.25
15065.93	1148.00	1140.12	-7.88
15145.92	1204.00	1184.85	-19.15
15427.47	1334.00	1320.82	-13.18
15801.45	1519.00	1518.99	-0.01
15829.66	1530.00	1532.57	2.57
15960.41	1608.00	1606.15	-1.85
16016.58	1637.00	1633.56	-3.44
16197.20	1732.00	1734.57	2.57
15469.94	1337.00	1334.33	-2.67
15438.92	1319.00	1316.72	-2.28
15338.93	1262.00	1262.07	0.07
15215.50	1196.00	1194.90	-1.10
15246.26	1218.00	1211.36	-6.64
15326.76	1251.00	1254.99	3.99
14944.11	1049.00	1049.89	0.89
14803.87	976.00	975.37	-0.63
14782.98	971.00	965.25	-5.75
14692.60	917.00	917.88	0.88
14563.63	849.00	848.41	-0.59

Table 6-2. Accuracy of the registration of GCPs (Continued).

x	x_{ref} (pixels)	x_{fit} (pixels)	Error (pixels)
14174.82	636.00	642.65	6.65
14255.32	685.00	684.05	-0.95
13806.38	449.00	448.57	-0.43

y	y_{ref} (pixels)	y_{fit} (pixels)	Error (pixels)
9029.81	1274.00	1273.78	-0.22
10839.32	260.00	267.20	7.20
10758.94	331.00	311.86	-19.14
10647.04	365.00	376.65	11.65
10548.19	434.00	428.17	-5.83
10486.92	475.00	463.98	-11.02
10235.79	607.00	602.26	-4.74
10244.13	592.00	600.88	8.88
10062.87	689.00	701.09	12.09
9982.62	745.00	744.78	-0.22
9959.43	756.00	762.79	6.79
9729.84	888.00	885.48	-2.52
9808.04	834.00	846.50	12.50
9536.02	993.00	995.44	2.44
9302.09	1116.00	1126.06	10.06
9117.25	1237.00	1230.63	-6.37
9116.23	1239.00	1232.37	-6.63
8452.58	1591.00	1586.75	-4.25
7977.77	1843.00	1839.49	-3.51
7837.40	1915.00	1912.75	-2.25
7895.74	1868.00	1883.86	15.86
7595.00	2046.00	2040.27	-5.73
7642.69	2014.00	2017.33	3.33
7861.99	1892.00	1895.45	3.45
7782.38	1938.00	1936.27	-1.73
7783.66	1936.00	1934.14	-1.86
7515.21	2069.00	2070.78	1.78
7574.82	2037.00	2040.58	3.58
7613.80	2019.00	2021.74	2.74
7408.67	2132.00	2120.83	-11.17

Table 6-2. Accuracy of the registration of GCPs (Continued).

y	y_{ref} (pixels)	y_{fit} (pixels)	Error (pixels)
7390.46	2123.00	2127.52	4.52
7320.72	2162.00	2162.85	0.85
7291.87	2183.00	2175.80	-7.20
7373.52	2124.00	2131.29	7.29
7468.49	2079.00	2073.78	-5.22
7507.46	2050.00	2055.69	5.69
7593.20	2000.00	2000.42	0.42

SECTION 7

DISCUSSION

Because only very limited ground truth is available for comparison with the results of this study, it is difficult to verify the accuracy of the stress maps that were produced. The 1987 gamma dose rate contours seem to correlate well with the later stress maps (Figure 5-18b), but the correlation is not perfect.

There are several important points to be made concerning these contours. First, the contours correspond to the gamma dose rate at a time (1 May 1987) approximately 1 year after the accident and not to the accumulated dose. Second, these contours show only the gamma dose rate, not the alpha or beta particle dose rates. Third, as discussed above, the position or these contours is probably not very accurate. In fact, for these reasons, the forest response can be considered to provide a more accurate indication of the integrated dose to foliage than do the 1 May 1987 dose contours.

There is one final noteworthy point concerning the position of the contours. It is possible that Soviet mitigation efforts were more effective over the damaged reactor than over the neighboring undamaged reactor. In that case, the center of the 100 mR/hr dose contour might really belong over the undamaged reactor. Mitigation efforts might also help to explain the southerly displacement of the dose contours relative to the areas of forest showing the highest stress (Figure 5-18). Much of the area that first showed stress, and that was later removed, lies outside the 100 mR/hr dose contour.

In lieu of ground truth, other methods for checking the results of this study can be applied to increase confidence in the results. Are the stress maps consistent with Soviet mitigation efforts in the area? Are the results self-consistent over time? Do the results of this study agree with those of other similar studies?

The first of these questions was addressed in considerable detail in Section 5. Basically, most Soviet mitigation efforts in forested areas appear to have been consistent with the stress map. The only notable exception was the northern edge of the coniferous forest located to the south of the reactor. This area consistently showed stress in the stress maps, but no signs of mitigation were evident. Some possible explanations are (1) that the Soviets may believe that this area will recover, (2) the area may have low priority for current operations, or (3) the afflicted area is too large for mitigation to be practicable.

With the exception of the winter months (when stress seems less detectable in the present analysis), the stress maps appear to be consistent with one another. The discolored area visible on the 29 April 1986 stress map is the same area that appeared stressed on the 8 May 1986 stress map.

Similarly, the stressed area on 24 May 1986 includes all the stressed areas of 8 May 1986. The 24 May 1986 and the 31 May 1986 stress maps show little difference. The stressed area of 11 May 1987 subsumes that in all the previous images. In addition, apart from that for the winter months, the effects measured by the stress index increased fairly uniformly with time. Thus, the stress maps are consistent with one another.

The last question is somewhat more difficult to address because of the lack of similar studies. Although the scope and even the data used for the study by Goldman and coworkers (Goldman, et al., 1987) were similar to that of the present work, the approaches and the results obtained were quite different. A comparison of the results obtained by these two studies is shown in Table 7-1. Most of the aspects of this comparison were discussed either above or in Section 5. In their study, a group of analysts (albeit experienced) attempted to identify stress visually by looking at photographic prints. Such a process is obviously subjective. Photographic prints are far from an ideal media, for the very production of the prints tends to involve variables usually controlled by subjective judgments (e.g., exposure and color balance). In addition, the dynamic range that can be achieved with the photographic process is not very large, resulting in a loss of information. In contrast, the results of this work were obtained largely by quantitative means. In this respect, we believe the methods and results of this study speak for themselves.

Johnson (1989) has developed a phenomena-based image-enhancement transformation that is gaining popularity in the intelligence community. Designed to detect a specific spectral manifestation of stress (the decrease in reflectance in TM band 4 and concomitant increase in reflectance in band 5), the transformation squares each pixel's intensity in band 4 and divides that by the pixel's intensity in band 5 (i.e., $4^2/5$). The transformed data are displayed as a color composite image ($4^2/5$ as red, band 4 as green, and band 5 as blue).

Table 7-1. Comparison of present work with that of Goldman and coworkers (1987).

Technique/result	Present work	Goldman and coworkers
Algorithm type	Change detection	Normalized difference vegetation index
Data preparation	Image registration	Spatially filtering image sharpening
Method of injury assessment	Quantitative (algorithmic)	Qualitative (visual)
First detectable change	8 May 1986 (12 days)	16 June 1986 (51 days)
Latest significant change	11 May 1987 (1 year)	15 October 1986 (5.6 months)

Care must be exercised in the interpretation of such single-date composite images. For example, one interpretation of a $4^2/5,4,5$ composite of the 11 May 1987 image of the Chernobyl area has vast new areas of forest beginning to show stress. Figure 7-1 shows this composite image. The area of stressed foliage indicated by our analysis (Figure 5-18) shows as a dark gray band in Figure 7-1. Johnson interprets the forest patches along the middle and upper left edge of the image as also being stressed. These purportedly newly stressed forested areas appear darker in the composite image than do other "unstressed" forest areas.

This interpretation is based in part on the assumption that this pattern did not appear on any imagery dated before 11 May 1987 and that the darkened forest should appear the same as the undarkened. However, comparing the forest classification map (Figure 5-1), which was derived from the 6 June 1985 image, with the color composite in Figure 7-1 suggests that the pattern actually did exist a year before the accident. To make this comparison easier, the boundaries of forested areas classified as being similar to training site 4 are colored white; all other forested regions are classified as being similar to training site 3. Figure 7-2, showing this outline overlaid on the composite, indicates that these supposedly newly stressed areas seem to correspond to areas covered by a different forest type rather than to the radiation dose contours published by the Soviets. In other words, the apparent stress is likely an artifact of the analysis rather than an effect of the radiation release. Indeed, a similar composite image shown in Figure 7-3 derived from the preaccident image of 6 June 1985 shows the same darkening pattern as the 11 May 1987 composite; therefore, the slightly dark appearing forest cannot be a new manifestation of radiation induced stress.

Dose estimates based on our analysis are not presented in this interim report. Such estimates will depend on being able to relate the radiation dose either to the spectral manifestations of stress or to the times at which these manifestations first became detectable. Dose rate may complicate the relationship by affecting the spectral characteristics of injury as well as of the dose-response time. Also, the question of the relative proportion of beta dose versus gamma dose requires careful examination. These issues will be addressed in the final report for this project.

Figure 7-1. Date: 11 May 1987, enhanced image; 4^2/5,4,5 false color.

Figure 7-2.   Boundaries of areas classified as similar to training site 4 overlaid on the
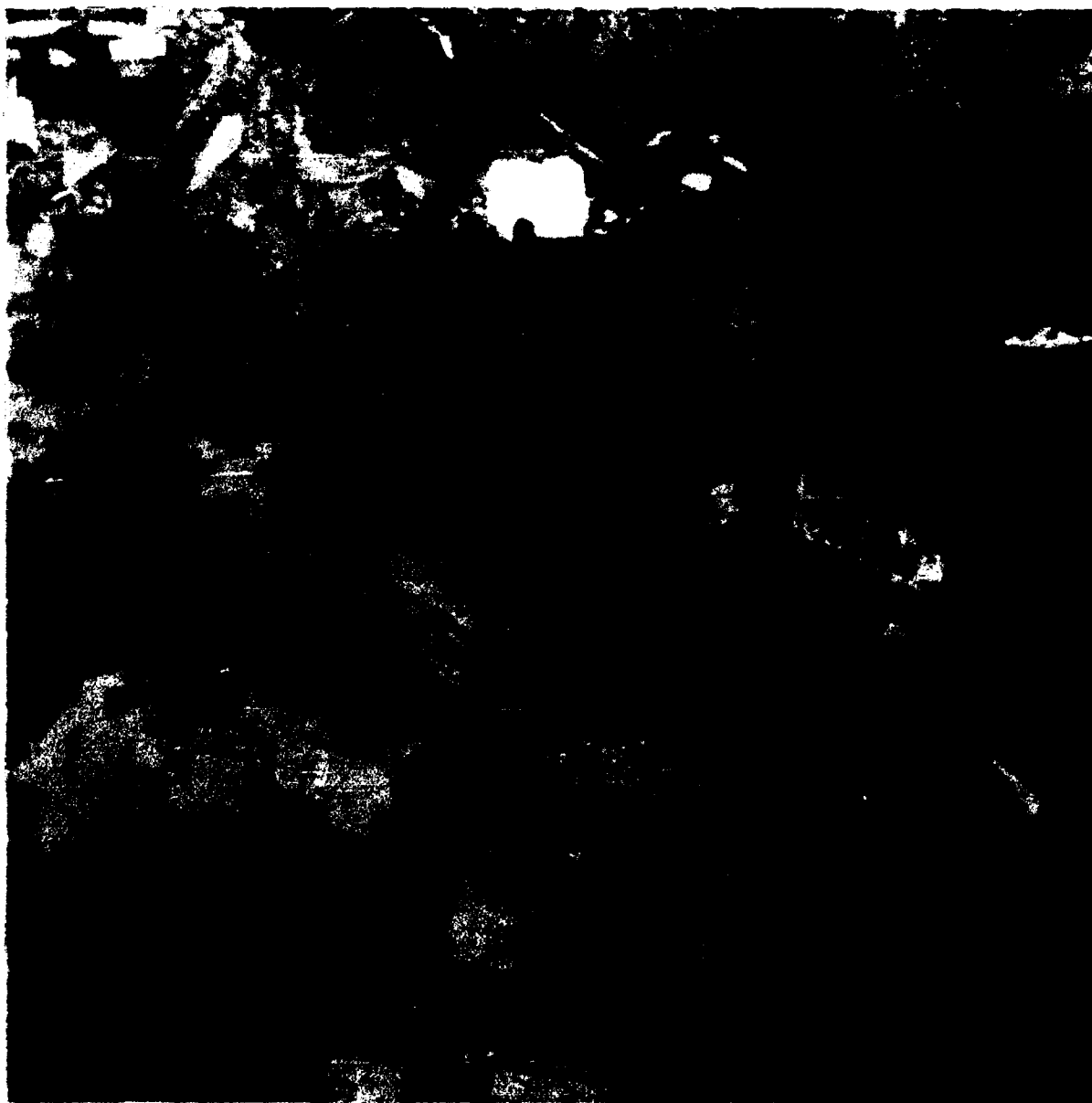11 May 1987 enhanced image; $4^2/5,4,5$ false color.

Figure 7-3. Date: 6 June 1985, preaccident image with the same image enhancement
transformation shown in Figure 7-1. Darker forested areas in this enhancement
correspond to a different forest type rather than to radiation damaged areas.

SECTION 8

CONCLUSION

Perhaps the most significant conclusion that can be drawn from this work is that remotely collected, low-resolution multispectral data can be used to identify radiation stressed foliage and to monitor it quantitatively. Furthermore, this capability is aided by the availability of a sensitive change detection algorithm, Hyperscout, that can detect this stress very early and reliably. Early detection is critical for accurate dose estimates.

When the data are in final form, a number of important results are anticipated. The first of these are estimates of the doses received by indigenous plant life. Secondly, the time history of the multispectral manifestations of various levels of radiation stress can be obtained, thus providing the first large-scale spectral measurements of the effects of a full range of radiation doses on conifers. This database would facilitate monitoring future accidents or even determining whether an accident had occurred. Such a database is not readily available from any other source.

Much work remains to be done. The most important task remaining is to estimate radiation dose from the foliage response. Once the stress maps are finalized, the spectral changes corresponding to various levels of stress will be determined. These spectral histories, in turn, will be used to estimate the health of the conifers. Finally, these health histories will be used to infer dose estimates.

Once dose estimates have been obtained, the process can be inverted. That is, the temporal aspects of the spectral manifestations of various levels of radiation stress can be extracted from the data.

Continued monitoring of the area is recommended for at least two reasons. First, the identification of new areas showing stress would expand the area for which dose estimates are available. This new dose information might be incorporated to refine the estimates of dose levels received by human populations. Second, but not unrelated, lightly stressed forests should be monitored for evidence of recovery. Again, the primary goal is the refinement of dose estimates. Of equal importance is the collection of spectral information not available from other sources.

Obtaining accurate dose estimates is the primary goal, and accurate determination of the dates of various stages of injury to the conifer community is required to obtain these estimates. There are available no high quality TM data for the period extending from 8 May 1986 to 24 May 1986, nor from 31 May 1986 to 15 October 1986. Yet, most of the spectral manifestations of the stress appear to have occurred during these two time intervals, while there seems to have been little change between 24 May 1986 and 31 May 1986. Because of the lack of suitable TM images, the question arises as to whether any other sources of multispectral data can be used to fill in these two

64

critically important gaps. The algorithm used in this work can detect and map stress using data from any sensor, provided the data are sufficiently complete. Thus, both SPOT and MSS data should be considered potentially useful for filling in these gaps, provided that the analysis requires neither SWIR nor LWIR data.

Another potentially useful approach to determining stress is to use TM data that was acquired at night. Night data should be much more sensitive to thermal stress. Thermal stress may be detectable much earlier than other forms of stress. If so, it could prove extremely valuable for detecting and monitoring the early stages of stress and, thus, for estimating dose.

There are also two modifications in processing that should be considered. First, instead of using the same reference image for all analyses, as was done in this study, the reference date should be chosen to correspond to the season of the image being analyzed. This may significantly improve the accuracy of the resulting stress map. For example, the 15 October and 2 December 1986 dates would be referenced to the 21 March 1986 date instead of the 6 June 1985 date. Unfortunately, snow cover present in the 21 March 1986 image may have a negative impact.

The second processing modification involves using the first three components of the Tasselled Cap transformation (Crist, Laurin, and Cicone, 1986) instead of bands 7, 4, and 3. The fourth component, usually referred to as "Haze," might also allow the automatic elimination of distracting areas of apparent change attributable to cloud cover or haze.

Extensions or alternatives to current algorithms should be investigated in the hope that even more sensitive algorithms may be found. One alternative is the use of neural networks to identify stress areas. Another promising area to explore is the simultaneous investigation of several (instead of just two) dates of imagery. This multitemporal processing might significantly improve the accuracy of the stress maps by removing the effects of noise and less than perfect registration.

The final kinds of potential improvement are aesthetic. Some such kinds of improvement include the removal of areas contaminated by cloud, cloud-shadow, or haze from consideration, because these areas spuriously produce high stress values and confuse the presentation. In like manner, measures could be developed to the remove edge effects and to reduce noise by mode or other filtering.

SECTION 9

REFERENCES

Asmolov, V.G., et. al., 1987
"The Accident at the Chernobyl Nuclear Power Plant: One Year After," International Atomic Energy Agency, IAEA-CN-48/63.

Crist, E.P., R. Laurin, and R.C. Cicone, 1986
"Vegetation and Soils Information Contained in Transformed Thematic Mapper Data," *Proceedings of IGARSS 1986 Symposium*, Zurich, 8-11 September 1986, pp.1465-1470.

Engel, J., 1984
"Thematic Mapper (TM) Instrument Description," *LANDSAT-4 Science Investigations Summary*, Vol. 1, NASA Conference Publication 2326, pp. 41-61.

Estes, J. E., Ed., 1983
Manual of Remote Sensing, Vol. II (American Society of Photogrammetry), pp. 1511-1513 and 2136-2187.

Goldman, M., et al., 1987
"Radiation Exposure Near Chernobyl Based on Analysis of Conifer Injury Using Thematic Mapper Satellite Images," University of California, Davis, California 95616 (unpublished).

Hoffer, R. M., 1978
"Biological and Physical Considerations in Applying Computer-Aided Analysis Techniques to Remote Sensor Data," *Remote Sensing: The Quantitative Approach*, edited by P. H. Swain and S. M. Davis (McGraw-Hill, New York) pp. 227-289.

Irons, J., 1985
"An Overview of LANDSAT-4 and the Thematic Mapper," *LANDSAT-4 Science Characterization Early Results*, Vol. II, NASA Conference Publication 2355, pp. 15-46.

Johnson, A. J., 1989
Central Intelligence Agency, Washington, D.C. 20505, private communication.

Matson, M., and J. Dozier, 1981
"Identification of Subresolution High Temperature Sources Using a Thermal IR Sensor," *Photogrammetric Engineering and Remote Sensing*, 47(9):1311-1318.

Swain, P.H., 1978
"Fundamentals of Pattern Recognition in Remote Sensing," *Remote Sensing: The Quantitative Approach*, edited by P. H. Swain and S. M. Davis (McGraw-Hill, New York) pp. 136-187.

Westman, W.E. and C.V. Price, 1988
"Spectral Changes in Conifers Subjected to Air Pollution and Water Stress: Experimental Studies," *IEEE Transactions on Geoscience and Remote Sensing*, 26(1): 11-21.

Whicker, F.W., and L. Fraley, Jr., 1974
Effects of Ionizing Radiation on Terrestrial Plant Communities, Vol. 4 of *Advances in Radiation Biology*, edited by J.T. Lett, H. Adler, and M. Zelle (Academic Press, New York).

Wiebelt, J.A., and J.B. Henderson, 1976
     Techniques and Analysis of Thermal Infrared Camouflage in Foliated Backgrounds (U.S.
     Army Mobility Equipment Research and Development Command), AD A038186.

Wolfe, W. L., and G. J. Zissis, eds., 1978
     The Infrared Handbook (Environmental Research Institute of Michigan), p. 3-140.

67

DISTRIBUTION LIST

DNA-TR-92-37-V2

DEPARTMENT OF DEFENSE

ARMED FORCES RADIOBIOLOGY RSCH INST
    ATTN: DEPT OF RADIATION BIOCHEMISTRY
    ATTN: BHS
    ATTN: DIRECTOR
    ATTN: EXH
    ATTN: MRA
    ATTN: PHY
    ATTN: RSD
    ATTN: SCIENTIFIC DIRECTOR
    ATTN: TECHNICAL LIBRARY

ASSISTANT SECRETARY OF DEFENSE
INTERNATIONAL SECURITY POLICY
    ATTN: NUC FORCES & ARMS CONTROL

ASSISTANT TO THE SECRETARY OF DEFENSE
    ATTN: EXECUTIVE ASSISTANT
    ATTN: MIL APPL C FIELD

DEFENSE INTELLIGENCE AGENCY
    ATTN: DB
5 CYS ATTN: DB-4 RSCH RESOURCES DIV
    ATTN: DB-5C
    ATTN: DB-6B
    ATTN: DB-6E
    ATTN: DIA/VPA-2
    ATTN: DIW-4
    ATTN: DN
    ATTN: DT
    ATTN: OFFICE OF SECURITY
    ATTN: OS

DEFENSE INTELLIGENCE COLLEGE
    ATTN: DIC/RTS-2
    ATTN: DIC/2C

DEFENSE LOGISTICS AGENCY
    ATTN: COMMAND SECURITY OFC

DEFENSE NUCLEAR AGENCY
    ATTN: CID
    ATTN: DFRA JOAN MA PIERRE
    ATTN: NANF
    ATTN: NASF
    ATTN: OPNA
    ATTN: OPNS
    ATTN: RAEE
20 CYS ATTN: RARP
2 CYS ATTN: TITL

DEFENSE TECHNICAL INFORMATION CENTER
2 CYS ATTN: DTIC/FDAB

FIELD COMMAND DEFENSE NUCLEAR AGENCY
    ATTN: FCPR
    ATTN: FCPRT
    ATTN: NUC SECURITY

FIELD COMMAND DEFENSE NUCLEAR AGENCY
    ATTN: FCNM

INTERSERVICE NUCLEAR WEAPONS SCHOOL
    ATTN: TTV
2 CYS ATTN: TTV 3416TH TTSQ

JOINT DATA SYSTEM SUPPORT CTR
    ATTN: C-332
    ATTN: JNSV

NATIONAL DEFENSE UNIVERSITY
    ATTN: ICAF TECH LIB
    ATTN: NWCLB-CR
    ATTN: LIBRARY
    ATTN: STRAT CONCEPTS DIV CTR

NET ASSESSMENT
    ATTN: DOCUMENT CONTROL

OFC OF MILITARY PERFORMANCE
ASSESSMENT TECHNOLOGY
    ATTN: F HEGGE

PROGRAM ANALYSIS & EVALUATION
    ATTN: NAVAL FORCES
    ATTN: STRATEGIC PROGRAMS & TNF

STRATEGIC AND THEATER NUCLEAR FORCES
    ATTN: DR E SEVIN
    ATTN: DR SCHNEITER

THE JOINT STAFF
    ATTN: JKAC
    ATTN: JLT
    ATTN: JPEP

THE JOINT STAFF
    ATTN: ED30 J-3 STRATEGIC OPS DIV
    ATTN: J-3 SPECIAL OPERATIONS
    ATTN: J-8 S CONLIN
    ATTN: JAD/SFD
    ATTN: JSOA

U S EUROPEAN COMMAND/ECJ-6-DT
    ATTN: ECJ-6

U S EUROPEAN COMMAND/ECJ2-T
    ATTN: ECJ2-T

U S EUROPEAN COMMAND/ECJ3-CCD
    ATTN: ECJ-3

U S EUROPEAN COMMAND/ECJ4-LW
    ATTN: ECJ4-LW

U S EUROPEAN COMMAND/ECJ5-N
    ATTN: ECJ5-N

U S EUROPEAN COMMAND/ECJ7/LW
    ATTN: ECJ-7 LW

UNDER SEC OF DEFENSE FOR POLICY
    ATTN: DUSP/P
    ATTN: USD/P

DEPARTMENT OF THE ARMY

COMBAT MATERIAL EVAL ELEMENT
    ATTN: SECURITY ANALYST

DEP CH OF STAFF FOR OPS & PLANS
    ATTN: DAMO-SWN
    ATTN: DAMO-ZXA

HARRY DIAMOND LABORATORIES
    ATTN: SLCH-NW-RS JOSIP SOLN
    ATTN: SLCIS-IM-TL

JOINT SPECIAL OPERATIONS COMMAND
    ATTN: J-2
    ATTN: J-5

NUCLEAR EFFECTS DIVISION
    ATTN: STEWS-NE-T

U S ARMY AIR DEFENSE ARTILLERY SCHOOL
    ATTN: COMMANDANT

U S ARMY ARMAMENT RSCH DEV & ENGR CTR
    ATTN: DRDAR-LCN-F

U S ARMY ARMOR SCHOOL
    ATTN: ATSB-CTD
    ATTN: TECH LIBRARY

U S ARMY BALLISTIC RESEARCH LAB
    ATTN: SLCBR-D
    ATTN: SLCBR-DD-T
    ATTN: SLCBR-TB
    ATTN: SLCBR-VL-I DR KLOPCIC
    ATTN: SLCBR-VL-V

U S ARMY COMBAT SYSTEMS TEST ACTIVITY
    ATTN: JCHN GERDES
    ATTN: MIKE STANKA

U S ARMY COMD & GENERAL STAFF COLLEGE
    ATTN: ATZL-SWJ-CA
    ATTN: ATZL-SWT-A

U S ARMY CONCEPTS ANALYSIS AGENCY
    ATTN: TECHNICAL LIBRARY

U S ARMY FIELD ARTILLERY SCHOOL
    ATTN: ATSF-CD

U S ARMY FORCES COMMAND
    ATTN: AF-OPTS

U S ARMY FOREIGN SCIENCE & TECH CTR
    ATTN: C WARD

U S ARMY INFANTRY CENTER
    ATTN: ATSH-CD-CSO

U S ARMY ITAC
    ATTN: IAX-Z

U S ARMY LABORATORY COMMAND
    ATTN: DIRECTOR
    ATTN: DR D HODGE

U S ARMY MATERIAL COMMAND
    ATTN: DRCDE-D

U S ARMY NUCLEAR & CHEMICAL AGENCY
    ATTN: MONA-NU
4 CYS ATTN: MONA-NU DR D BASH

U S ARMY TEST & EVALUATION COMMAND
    ATTN: STECS-NE

U S ARMY WAR COLLEGE
    ATTN: LIBRARY
    ATTN: STRATEGIC STUDIES INSTITUTE

U S MILITARY ACADEMY
    ATTN: BEHAVORIAL SCI & LEADERSHIP
    ATTN: COL J G CAMPBELL
    ATTN: SCIENCE RESEARCH LAB

US ARMY MATERIEL SYS ANALYSIS ACTVY
    ATTN: DRXSY-DS

USA SURVIVABILITY MANAGMENT OFFICE
    ATTN: SLCSM-SE J BRAND

USACACDA
    ATTN: ATZL-CAD-N

DEPARTMENT OF THE NAVY

DEPARTMENT OF THE NAVY
    ATTN: PMS-423
    ATTN: SEA-06GN

MARINE CORPS
    ATTN: CODE PPO
    ATTN: PSI G RASP

NAVAL OCEAN SYSTEMS CENTER
    ATTN: CODE 9642-B

NAVAL PERSONNEL RES & DEV CENTER
    ATTN: CODE P302

NAVAL POSTGRADUATE SCHOOL
    ATTN: CODE 1424 LIBRARY

NAVAL RESEARCH LABORATORY
    ATTN: CODE 1240
    ATTN: CODE 2627

NAVAL SURFACE WARFARE CENTER
    ATTN: CODE F-31
    ATTN: G RIEL

NAVAL TECHNICAL INTELLIGENCE CTR
    ATTN: NTIC-DA30

NAVAL WAR COLLEGE
    ATTN: CODE E-11
    ATTN: CTR FOR NAV WARFARE STUDIES
    ATTN: DOCUMENT CONTROL
    ATTN: LIBRARY
    ATTN: STRATEGY DEPT

NAVAL WEAPONS EVALUATION FACILITY
    ATTN: CLASSIFIED LIBRARY

NUCLEAR WEAPONS TNG GROUP, ATLANTIC
 ATTN: CODE 222
 ATTN: DOCUMENT CONTROL

NUCLEAR WEAPONS TNG GROUP, PACIFIC
 ATTN: CODE 32

OFFICE OF CHIEF OF NAVAL OPERATIONS
 ATTN: NIS-22
 ATTN: NOP 06D
 ATTN: NOP 403
 ATTN: NOP 50
 ATTN: NOP 60
 ATTN: NOP 60D
 ATTN: NOP 603
 ATTN: NOP 91
 ATTN: OP 654
 ATTN: PMS/PMA-423

OPERATIONAL TEST & EVALUATION FORCE
 ATTN: COMMANDER

PLANS, POLICY & OPERATIONS
 ATTN: CODE-P
 ATTN: CODE-POC-30

TACTICAL TRAINING GROUP, PACIFIC
 ATTN: COMMANDER

DEPARTMENT OF THE AIR FORCE

ACADEMY LIBRARY DFSELD
 ATTN: LIBRARY

AFIS/INT
 ATTN: INT

AIR UNIVERSITY
 ATTN: STRATEGIC STUDIES

AIR UNIVERSITY LIBRARY
 ATTN: AUL-LSE
 ATTN: LIBRARY

ASSISTANT CHIEF OF STAFF
2 CYS ATTN: AF/SAMI

ASSISTANT CHIEF OF THE AIR FORCE
 ATTN: SAF/AQA

DEPUTY CHIEF OF STAFF PLANS & OPERS
 ATTN: AFXOOSS

FOREIGN TECHNOLOGY DIVISION
 ATTN: CCN
 ATTN: SDA

TACTICAL AIR COMMAND/XPSC
 ATTN: TAC/DOA

USAF SCHOOL OF AEROSPACE MEDICINE
 ATTN: RADIATION SCIENCES DIV

DEPARTMENT OF ENERGY

DEPARTMENT OF ENERGY
 ATTN: DR T JONES

LAWRENCE LIVERMORE NATIONAL LAB
 ATTN: Z DIVISION LIBRARY

LOS ALAMOS NATIONAL LABORATORY
 ATTN: D STROTTMAN
 ATTN: REPORT LIBRARY

MARTIN MARIETTA ENERGY SYSTEMS INC
 ATTN: B SANTORO
 ATTN: G KERR
 ATTN: J WHITE
 ATTN: W RHOADES

SANDIA NATIONAL LABORATORIES
 ATTN: TECH LIB 3141

OTHER GOVERNMENT

CENTRAL INTELLIGENCE AGENCY
 ATTN: COUNTER TERRORIST GROUP
 ATTN: DIRECTOR OF SECURITY
 ATTN: MEDICAL SERVICES
 ATTN: NIO-T
 ATTN: N10 STRATEGIC SYS

FEDERAL EMERGENCY MANAGEMENT AGENCY
 ATTN: CIVIL SECURITY DIVISION
 ATTN: G ORRELL NP-CP
 ATTN: R SANDS

U S DEPARTMENT OF STATE
 ATTN: PM/STM

U S NUCLEAR REGULATORY COMMISSION
 ATTN: DIR DIV OF SAFEGUARDS
 ATTN: S YANIV

DEPARTMENT OF DEFENSE CONTRACTORS

ARES CORP
 ATTN: A DEVERILL

HORIZONS TECHNOLOGY, INC
 ATTN: F GREY

HORIZONS TECHNOLOGY, INC
 ATTN: J MARSHALL-MIES

KAMAN SCIENCES CORP
 ATTN: DASIAC

KAMAN SCIENCES CORPORATION
 ATTN: R STOHLER

KAMAN SCIENCES CORPORATION
 ATTN: DASIAC

LOCKHEED MISSILES & SPACE CO, INC
 ATTN: WE-YOUNG WOO

LOGICON R & D ASSOCIATES
 ATTN: DOCUMENT CONTROL
 ATTN: DOUGLAS C YOON

LOGICON R & D ASSOCIATES
 ATTN: S WOODFORD

MICRO ANALYSIS AND DESIGN
        ATTN: R LAUGHERY

MISSION RESEARCH CORP
        ATTN: DR NEIL GOLDMAN

PACIFIC-SIERRA RESEARCH CORP
 2 CYS ATTN: G ANNO
12 CYS ATTN: G E MCCLELLAN
        ATTN: H BRODE
 2 CYS ATTN: R N DEWITT
 2 CYS ATTN: T H HEMMER

PACIFIC-SIERRA RESEARCH CORP
        ATTN: D GORMLEY
 2 CYS ATTN: G MCCLELLAN

SCIENCE APPLICATIONS INTL CORP
        ATTN: D KAUL
        ATTN: E SWICK
        ATTN: L HUNT
        ATTN: R J BEYSTER
        ATTN: W WOOLSON

SCIENCE APPLICATIONS INTL CORP
        ATTN: B BENNETT
        ATTN: D BAREIS
        ATTN: J FOSTER
        ATTN: J MCGAHAN
        ATTN: J PETERS
        ATTN: W LAYSON

SCIENCE APPLICATIONS INTL CORP
        ATTN: R CRAVER

SCIENCE APPLICATIONS INTL CORP
        ATTN: JOHN A SHANNON

TECHNICO SOUTHWEST INC
        ATTN: S LEVIN

TRW OGDEN ENGINEERING OPERATIONS
        ATTN: D C RICH

TRW SPACE & DEFENSE SECTOR
        ATTN: DR BRUCE WILSON

UNIVERSITY OF CINCINNATI MEDICAL CENTER
        ATTN: E SILBERSTEIN